THE STUDY OF DNA DYNAMICS AT CARBON ELECTRODE SURFACE TOWARD DNA SENSORS BY FLUORESCENCE AND ELECTROCHEMICAL IMPEDANCE SPECTROSCOPY

by

QIN LI

B.S., Beijing Normal University, 2007

A THESIS

submitted in partial fulfillment of the requirements for the degree

MASTER OF SCIENCE

Department of Chemistry
College of Arts and Sciences

KANSAS STATE UNIVERSITY
Manhattan, Kansas

2011

Approved by:

Major Professor
JUN LI

Abstract

This study is focused on exploring the mechanisms of DNA dynamics at carbon electrode surfaces under a strong electric field for the development of novel DNA hybridization sensors.

Oligonucleotides with FAM6 attached at the distal end are covalently tethered on the carbon electrode surface. The fluorescence emission from the FAM6 is strongly quenched in close proximity to the electrode surface. The modulation to the fluorescence intensity is correlated with the reversible reorientation of the negatively charged DNA molecules under the electric field within the electric double layer. The orientation dynamics are apparently determined by the interplay of the electropotential, salt concentration, and stiffness of the DNA molecules. We have observed that dsDNAs switch with fast dynamics (in < 0.05 second) followed by relaxation at a slower rate (in > 0.1 second) when the electric field is altered by stepping the electropotential to a more positive or negative value. The DNA reorientation exhibits strong dependence on the PBS buffer concentration and electric double layer thickness. A preliminary calculation based on dipole-surface energy transfer theory indicates that the critical distance between FAM6 and glassy carbon surface is 10.95 nm.

In connection with the fluorescence study, the effect of DNA hybridization on electrochemical impedance spectroscopy (EIS) has also been investigated by two methods in an attempt to develop a fast electronic detection method. First, EIS at high AC amplitude (141 mV rms) with DNA-modified glassy carbon electrodes before and after target DNA hybridization have shown notable change at high frequencies, likely related to the DNA reorientation processes. Second, reversible EIS detection of DNA hybridization has been demonstrated with patterned regular carbon nanofiber arrays at normal AC amplitude (10 mV rms). The combination of these two methods will be explored in future studies.

The effects of the electric field on surface-tethered molecular beacons (MBs) have also been studied with fluorescence spectroscopy. An increase in fluorescence at negative bias is observed accompanying the opening of the MB stem, which leads to larger separation between fluorophore and quencher. At positive bias, the rehybridization of the MB stem leads to a decrease in fluorescence intensity.

Table of Contents

List of Figures

List of Tables

Acknowledgements

First and foremost, I would like to thank Dr. Jun Li and Dr. Daniel Higgins for supporting and supervising me throughout my Master's work. Without their patient discussion, encouragement and help in the lab, this work could not be possible. Second, I would like to thank Jeffrey Lange, Dr. Jianwei Liu, Chenchen Cui, Lateef syed, and Dr. Brue Gale's group at the University of Utah for their help on varies aspects with these projects. Third, I would like to thank my families and friends for their love and support all the time. Finally, I would like to thank the Chemistry Department of Kansas State University for this unique opportunity to study here, and Early Warning Inc. for partial financial support to this work.

Dedication

I dedicate this work to my families.

Chapter 1 - Introduction and significance

1.1Background introduction

Billions of dollars in economic loss and millions of illnesses are caused by contaminated food and water with pathogenic bacteria such as *E. coli* and *Salmonella*. [1] The year 2010 has witnessed more than half a billion eggs being recalled due to a salmonella outbreak, which has sickened hundreds of people.[2] To prevent and reduce potential losses resulting from pathogenic bacteria, early detection of their presence is of vital importance.[3] Traditional bacteria identification methods such as bacteria culture, immunological tests, and nucleic acid based molecular detection are laborious and time-consuming.[3] By using traditional detection methods, consumers may already have ingested and been infected by pathogens before the test results are known. Thus, an automated device that provides fast and accurate diagnosis of pathogens in field is highly demanded.

1.1.1 Brief introduction of DNA hybridization sensors

DNA sensors could be divided into two types: sensors that detect specific DNA hybridizations and sensors that detect DNA mutations. Optical and electrochemical transduction techniques have been utilized previously to develop DNA sensors.[4] The optical techniques include fluorescence detection, surface-enhanced Raman scattering spectroscopy, chemiluminescence, etc.[4] DNA microarrays are an important class of DNA hybridization sensors that employ optical detection methods. They have been widely used for gene expression and diagnosis in conjunction with gene sequencing propelled by the Human Genome Project since 1990. Electrochemical transduction could be based on either label or label-free methods.[4, 5] Electrochemically active species such as ferrocene could be directly attached to the probe or target to produce a signal.[4, 6] Label-free transduction relies on the oxidation of Guanine or the surface capacitance change upon hybridization of target DNA with surface functionalized probes.[7]

Due to the intrinsic properties of electrochemical methods, it is promising to develop low-cost, fast, handheld DNA detection platforms. Recently, Chen et al. employed differential pulse voltammetry (DPV) to detect the oxidation signal from 2-nitroacridone (NAD) at -0.116 V on a glassy carbon electrode surface (GCE). NAD had high electrochemical activity on bare GCE, but the activity decreased as the surface density of DNA increased.[8] Ozkan-Ariksoysal, et al. have designed a disposable DNA hybridization sensor specific for the catelchol-o-methyl transferase gene. In this work, Guanine containing target DNA was first attached onto a disposable graphite electrode and DPV was performed to measure Guanine oxidation. The decrease in DPV signal indicated probe DNA hybridization.[9] Zhang, et al. developed a novel DNA sensor by introducing ferrocene labeled probe into the sandwich system and then DPV and electrochemical impedance spectroscopy (EIS) were used to detect the hybridization event.[10]

Implementation of nanomaterials in electrochemical DNA sensors has also attracted significant attention recently. Nano-electrodes are classified as electrodes and have at least one dimension ranging from 1 nm to 100 nm.[11] They are very promising for elucidation of fundamental life behaviors such as DNA construction and neuron system regulation since they have similar sizes to active entities of these biosystems.[12-14] It is also possible to reduce the testing time by using arrays that combine thousands of nano-electrodes for higher measurement capacity.[12]

1.1.2 Electric double layer effects on DNA sensors

Current electrochemical DNA sensors usually employ a monolayer of probe DNA anchored on the working electrode surface.[5] When placed in electrolyte, electric double layer (EDL) will form at the electrode-solution interface. The EDL is comprised of a counterion gradient profile that forms near the electrode surface and screens the charge on the electrode surface produced by the potential bias. The thickness of the EDL is inversely proportional to the square root of the ionic strength of the electrolyte (Figure 1-1).[15, 16]

Rant et al. have studied the effects of the electric field in the EDL on DNA orientation dynamics in a number of recent publications.[17-24] DNA with Cy3 (Figure1-3) modified at the 5' end was tethered on a gold electrode surface through thiol-gold covalent binding. An electric field was applied to manipulate the orientation of the negatively charged DNA and the fluorescence signal was monitored throughout the procedure.

According to the Fö rster resonance energy transfer (FRET) theory, if the distance (d) between a donor and acceptor is less than 10 nm, the energy will transfer between them. And the efficiency is proportional to d^{-6} for nonradiative energy transfer. But if a dye molecule is placed near a metallic surface, both radiative and nonradiative resonant energy transfer (RET) take place.[25] Among the dye to metallic surface energy transfer situations, if d is smaller than 10 nm, the nonradiative process dominates. The electron gas of the surface absorbs the excitation energy through bulk scattering, metallic surface scattering and the spatial variation of dye itself. In this case, the energy transfer efficiency dependence on d is between d^{-4} and d^{-3}. For $d \leq 5$ nm, it is close to d^{-4}, and for $d \geq 5$ nm, it is close to d^{-3}.[26]

The traditional FRET or RET theory works only for distances less than 8 nm.[27-29] If the distance between dye and metallic surface is larger than 8 nm, the energy transfer will be weaker, and the energy transfer efficiency is d^{-4} dependence, which is called dipole-surface energy transfer (SET).[27, 30]

By taking advantage of RET theory, Rant et al. [19]designed their system (Figure 1-2) to utilize the fluorescence signal to investigate the DNA orientation relative to the gold surface under the influence of an electric field controlled by a potentiostat. In these experiments, a gold electrode modified with a mixed layer of dsDNA and mercaptohexanol (MCH) was placed in the light path of a 514 nm Ar^+ laser. The 560 nm emission from the dye label was collected by the spectrometer. The main interesting points of their research are summarized below:

First, the orientation of DNA could be controlled by the electric field in EDL. Negative potentials (-0.2 V vs. the open circuit potential (OCP)) repelled the negatively charged DNA, causing it to stand up, as was indicated by an increase in the observed fluorescence signal. Positive potentials (+0.2 V vs. OCP) attracted DNA to the electrode surface, causing it to lie down, as indicated by a decrease in the observed fluorescence signal. The strong electric field generated within the thickness of EDL could be used to manipulate DNA orientation because the electric field overwhelms the thermal energy.[19, 24]

Second, in the platform mentioned above, dsDNA and ssDNA showed different behavior under the influence of the electric field.[21] For positive potentials (DNAs lying down on the electrode), dsDNA and ssDNA showed nearly the same distance to the electrode surface; while for the negative potentials (DNA repelled from the electrode surface), ssDNA's height only reached 80% of that for dsDNA to the electrode surface. This phenomenon was attributed to the fact that only the lower portion of ssDNA is affected by electric field because of the flexibility of the ssDNA molecules and the quick decay of the electric field strength beyond the EDL. The persistence length of dsDNA is about 50 nm under the experimental salt concentration, but for ssDNA it is only about 2 nm.[20] Thus dsDNA behaves like a rigid rod, while ssDNA behaves as a flexible chain. The electric field is screened out by the ionic profile within the EDL, which results in strong electrostatic repulsion only acting on the 3'end of the DNA (the end that is anchored on the electrode surface). Detailed simulations were also performed by Rant, et al; in which they used Brownian dynamics simulations to simulate the DNA movement. The simulation results were in good agreement with the experimental data.[21, 23]

Third, the DNA orientation state on the electrode surface was correlated with the EDL charging and discharging, but lagged behind in time scale.[19] In 10 mM Tris buffer with 50 mM NaCl, the exponential fitting of the current – time profile showed that the double layer charging time was 38 µs, whereas the transition time of dsDNA switching was 45 µs.[21] The dsDNA reorientation time decreased as the ionic concentration increased. In another experiment, these authors scanned the potential modulation frequency from 100 kHz to 1 Hz and showed a cutoff frequency at 10 kHz for manipulating dsDNA orientation. The frequency response could be divided into three regions: for frequencies ≤ 1 kHz, there was large modulation; for frequencies between 1 kHz and 10 kHz, the modulation amplitude decreased; for frequencies ≥ 10 kHz, the modulation disappeared.[20] This experimental data further confirmed that the DNA orientation switching lags behind the EDL formation.

Fourth, parameters such as DNA length, ionic concentration, temperature, DNA density, electric field strength, etc. have been investigated systematically in Rant's studies. A 48-mer dsDNA showed stronger fluorescence signal modulation than 24-mer dsDNA, which could be theoretically supported by RET theory. In NaCl solution, for high salt concentrations (1000 mM), the dsDNA could seldomly be manipulated by the electric field while for medium salt concentrations (4 mM – 100 mM), the electric field manipulation effect decreased as the salt concentration increased. These results could be explained by the thickness of the EDL, which varies with the salt concentration.[18] The temperature mainly affected the manipulation of ssDNA.[18] Low density ≤ 10^{11} DNA/cm^2 was required to effectively manipulate DNA orientation.[17] Densities higher than this will have significant steric hindrance between neighboring molecules and reduced reorientation amplitudes.[20]

Beyond these basic studies, Rant, et al. also explored the application of this platform to the development of sensors for DNA hybridization [20] and for detection of proteins and their size through their effects on the fluorescence modulation amplitude.[22, 24] Rant's research results have demonstrated the importance of the EDL in manipulating DNA orientation. A more complete model for charged macromolecules that are anchored on an electrode surface and serve as a part of the EDL species, and their responses to the rearrangement of the EDL driven by an applied electropotential bias has not yet been obtained.

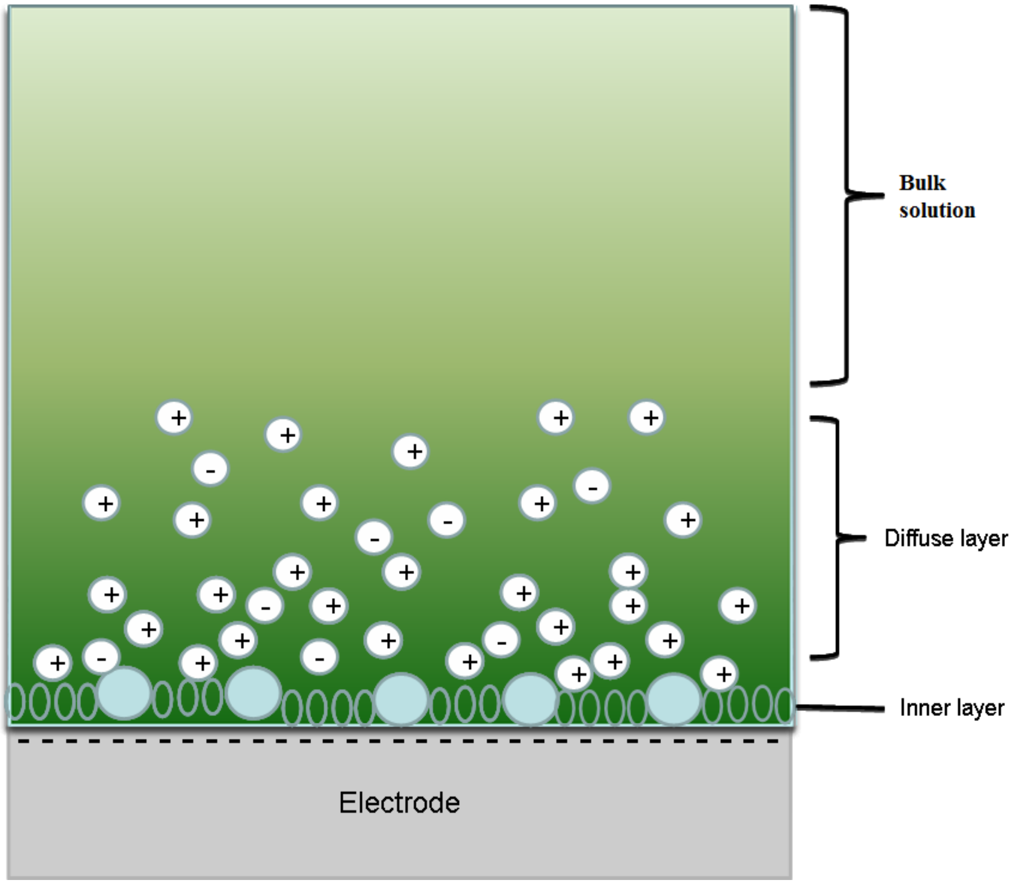

Figure 1-1 Stern modification of electric double layer formed at a negative biased electrode-solution interface.[16]

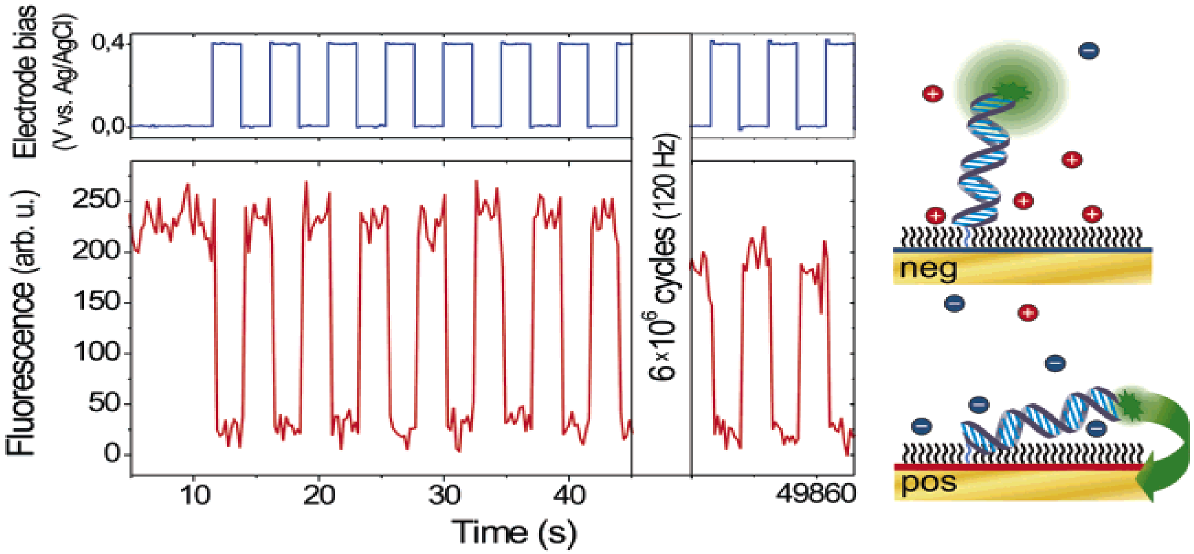

Figure 1-2 Plot of Rant's work [19] that shows the fluorescence signal response with the alternating potential step. The step height is 0.4 V vs. Ag/AgCl, and the frequency is 0.2Hz. Right shows the physical model of DNA switch driven by potential bias and the dependence of energy transfer efficiency of Cy3 to gold surface on the distance. (Adapted with permission from ref. 19. Copyright © 2004 American Chemical Society.)

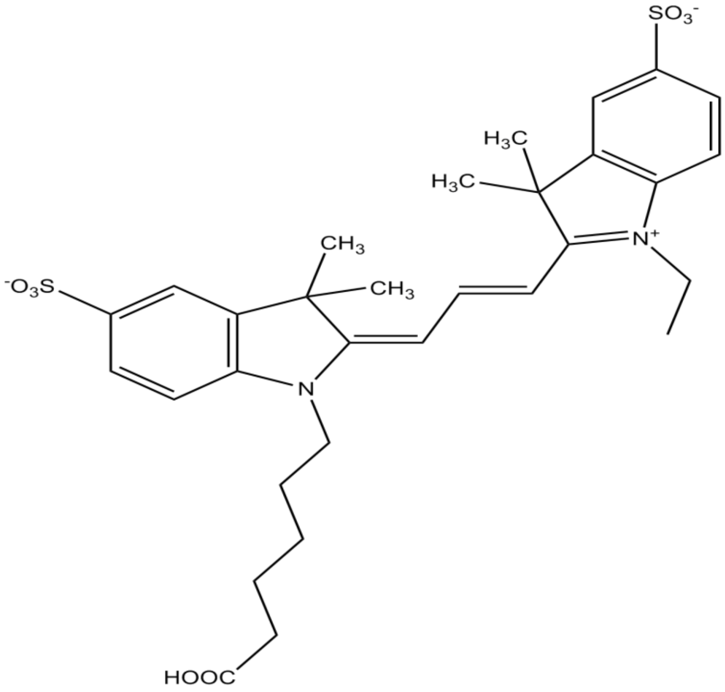

Figure 1-3 Structure of Cy3 in ref. 19.

1.1.3 Motivation of this study

Rant, et al. have shown that DNA hybridization could be detected by monitoring the electric field induced reorientation dynamics of dye labeled DNA anchored on a gold surface. Their platform requires a laser to excite the dye and a very sensitive camera to detect the emission photons, which is only doable in laboratory settings.

To develop a fast, portable and low-cost electronic DNA hybridization sensor based on label-free EIS measurements, we would like to first seek a full understanding of the mechanism of electric field induced DNA reorientation dynamics, which will lay the foundation for electronic detection methods. The studies performed under this thesis focus on exploring the role that the polycharged dsDNA plays in the reconstruction of the EDL and the impacts of the EDL on electric field induced dsDNA reorientation. Optical methods were used to probe the movement of dsDNA within the electric field of the EDL. Different ionic strengths were investigated to understand their impact of the EDL. In parallel, we utilized the mechanism of DNA reorientation driven by the electric field to develop a DNA hybridization detection method based on electronic signals alone using EIS.

1.2 Materials

1.2.1 Carbon electrode

Graphitic carbon based electrode consisting conductive sp^2-like carbons have been widely used in electrochemistry.[31] The microscopic structure of graphitic carbon suggests a basal plane parallels to the graphite plane, and an edge plane perpendicular to the graphite plane.[32] Both the electrochemical and chemical properties of basal plane and edge plane are very different. Electrochemically, cyclic voltammetry experiments in ferrocyanide solutions indicate that the electron transfer rate of edge plane pyrolytic graphite electrodes is more than 3 orders of magnitude faster than that of basal plane pyrolytic graphite electrodes.[33] Chemically, the basal plane is chemically inert due to the strong covalent bonds between sp^2 carbons; while edge plane is quite active since many functional groups such as phenols, quinones, carbonyl, and carboxylic acids are formed through oxidization of broken c-c bonds. The functional groups at the edge plane could be further oxidized or reduced to bond with other molecules under certain conditions.[34]

1.2.1.1 Glassy carbon

Glassy carbon is a kind of carbon made by pyrolyzing carbon precursors at high temperature.[35, 36] It is impermeable to gas or water, and chemically inert.[36, 37] Early research suggested a structure model that contains sp^3 (tetrahedral parts) and sp^2 (graphitic parts) carbons.[38] Later, Jenkins-Kawamura model suggested a structure model that contains thin ribbons of curved graphite sheets.[39] Recently, Harris proposed a model (Figure 1-4) that contains fullerene-like elements based on transmission electron microscopy analysis.[40, 41] This fullerene-like model contains microstructures such as multilayers of broken or imperfect fullerene-like nanostructures, and fully closed nanostructures. It could well explain glassy carbon's impermeability to gas or water as well as its inactivity to chemical reaction due to a high proportion of defect-free graphite basal plane like structures, and a low proportion of broken C-C bonds similar to the graphite edge plane.

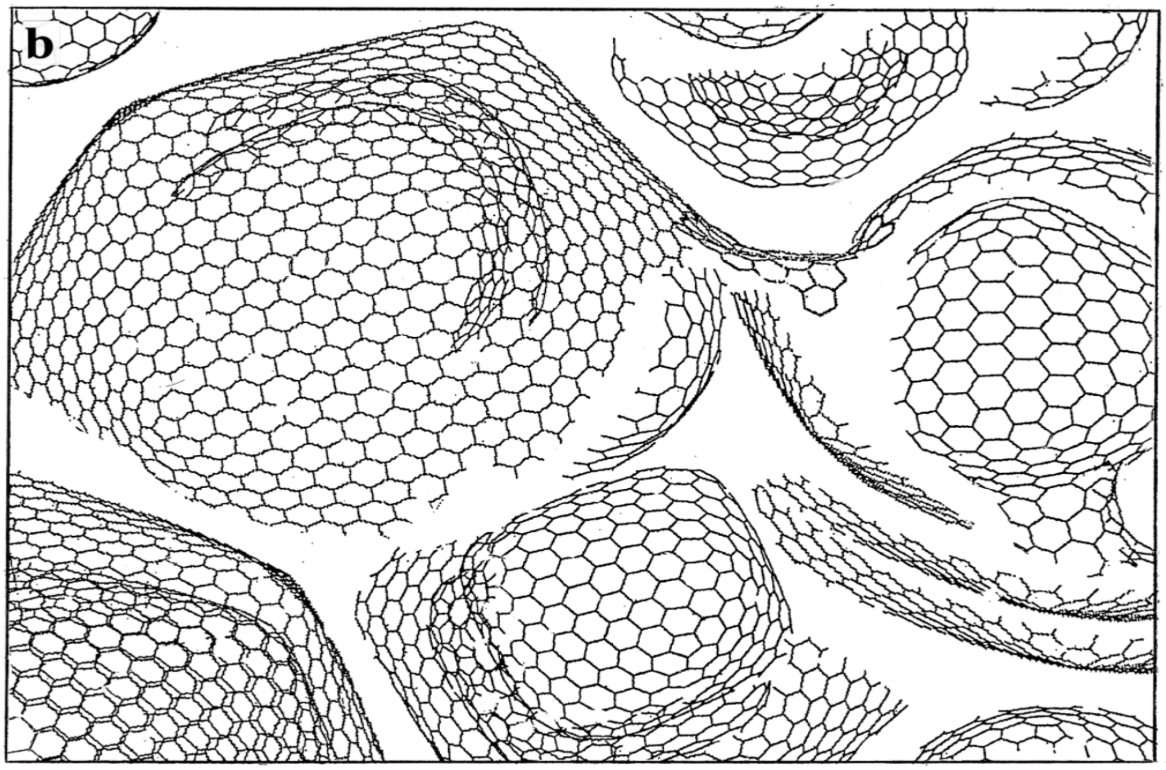

Figure 1-4 Structure of commercial glassy carbon proposed by Harris based on TEM studies. A fullerene like structure was first mentioned in this work, which could well explain the properties of glassy carbon such as the impermeablity to gas, chemically inreactivity.[41] (Adapted with permission from ref. 41. Copyright © 2004 Taylor & Francis.)

1.2.1.2 Vertically aligned carbon nanofibers (VACNF)

The first carbon nanotube sample was prepared in 1991.[42] Carbon nanotubes have since been applied to develop a wide range of biosensors. Carbon nanofibers (CNFs) are a kind of variation from carbon nanotubes which can be grown vertically on electrode surfaces. Inlaid VACNF arrays have been developed by Li, et al. as nanoelectrode arrays (NEAs) for electroanalysis[12, 43-47]. They applied tetraethyl orthosilicate (TEOS) chemical vapor deposition (CVD) to deposit a SiO_2 layer which insulates the CNF from neighboring CNFs as well as increasing their mechanical strength. The fabrication of inlaid VACNF array involves the following procedures: 1. Deposit a thin layer of Cr on a silicon substrate; 2. Deposit Ni catalyst on the Cr layer for the growth of VACNF; 3. Grow VACNFs by plasma enhanced chemical vapor deposition (PECVD) by reduction of C_2H_2; 4. Deposit a layer of SiO_2 to encapsulate the VACNF by TEOS CVD; 5. Expose the tips of VACNF as the desired density by reactive ion etching (RIE) and mechanical polish with polishing slurry.[43, 45, 46]

Li, et al. demonstrated that inlaid VACNF arrays with low density tip exposure responded 1000 time faster than common macroelectrode but generate the same magnitude of signal.[46] They applied their inlaid VACNFs to develop a DNA sensor based on DPV detection of Guanine oxidation.[44, 47, 48]

1.2.2 Hairpin DNA

Hairpin DNAs are also known as molecular beacons. These were first developed by Sanjay et al. in 1995.[49] They consist of a “stem-loop” structure formed by ssDNA. The stem part has two arms with complementary sequences in which the end of one arm is tagged with a fluorophore and the other one is tagged with a quencher.[49, 50] When the stem arms are hybridized with each other, the fluorophore is quenched by the quencher, and low fluorescence will be observed. While the two arms are separated apart from each other, the fluorophore gives strong fluorescence. Hybridizing a target with the loop part[49]or raising the temperature [51] will disassemble the “stem-loop” structure. Hairpin DNA has been widely used in detection of DNA or RNA in living cells,[52, 53] real-time PCR,[54] etc.

DNA in neutral solution is negatively charged. Strong electric fields can therefore be used to manipulate DNA in solution such as concentrating DNA at a positively biased electrode[55] or dehybridizing dsDNA with strong negative bias[56]. The strong electric field within the EDL generated by a negative bias should force open the stem arms of hairpin DNA that is anchored to the electrode at the quencher end.[56] After dehybridization, the arm with fluorophore should be repelled from the surface and fluoresce brightly (Figure 1-5).

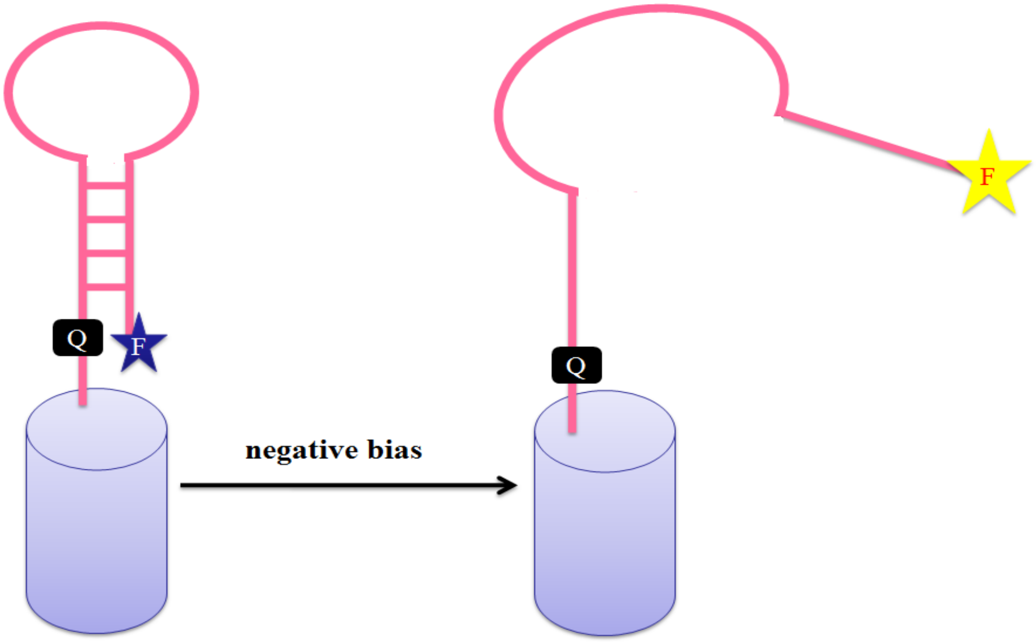

Figure 1-5 Schematic plot of dehybridization of hairpin DNA driven by the electric field.

1.3 Electrochemical methods

Numerous DNA electrochemical sensors have been introduced based on the redox reactions of DNA residues.[57] Adenine (A) and Cytosine (C) reduction signals were first used in oscillographic polarography. Guanine (G) could be oxidized at around 1.05 V (vs. SCE in pH=4.8 supporting electrolyte[44]) giving an anodic signal. Furthermore, the Guanine oxidation signal can be amplified by adding electrochemical mediators such as Ruthenium (II) bipyridyl chloride. But these redox reactions of DNA residues are irreversible.

1.3.1 Electrochemical Impedance Spectroscopy (EIS)

The EIS method not only detects DNA immobilization events with minimum damage to the biomolecules, but also provides the means for investigation of the interfacial phenomena, e.g. the structure change of DNA layer absorbed on the electrode surface and electron transfer mechanisms from the bulk solution to the electrode surface.[57-59] EIS has provided a possibility to develop fast, cheap, user-friendly DNA sensors for DNA hybridization.[60] Enormous efforts have been put on increasing the sensitivity (read out signal down to picomolar range) and the selectivity (distinguishing single-nucleotide mismatched ssDNA from the complementary ssDNA target) of EIS methods.[7]

EIS is also called AC impedance spectroscopy. The system impedance (Z) can be measured by applying modulated potentials over a large frequency range (1 MHz to 1 mHz) of small sinusoidal potential ($V(t) = V_0 * \sin(\omega t)$, with peak potential $V_0 \leq 50$ mV) to an electrochemical cell, while detecting the response current ($I(t) = I_0 * \sin(\omega t + \varphi)$). From the Euler relationship, the impedance (Z) can be represented as $Z = Z_0 * (\cos\varphi + j\sin\varphi)$, which includes a real part and an imaginary part:[61-63]

AC potential: $V(t) = V_0 * \sin(\omega t)$ **(1.1)**

Current response: $I(t) = I_0 * \sin(\omega t + \varphi)$ **(1.2)**

Impedance: $Z = {V(t)}/{I(t)}$ **(1.3)**

$$Z = Z_0 * (\cos\varphi + j\sin\varphi) \qquad \textbf{(1.4)}$$

EIS data is usually plotted as a Nyquist plot (the imaginary impedance vs. real impedance at discrete frequencies) or Bode plots (the total impedance or phase vs. logarithm of frequency). The EIS is usually modeled with an equivalent circuit incorporating 4 major components that represent the electrode-electrolyte interface: Resistor (R), capacitor (C), constant phase element (CPE) and Warburg impedance (Z_W).[61, 63] Except for resistor, the other three components have frequency dependent impedances.

As we know, if two components Z_1 and Z_2 are in series, the total impedance should be: $Z = Z_1 + Z_2$ (e.g. resistor (R) and capacitor (C) are in series, $Z = R - \frac{j}{\omega C}$, Figure 1-6-A depicts the computer simulated Nyquist plot of this circuit.);

If Z_1 and Z_2 are in parallel, the relationship should be: $\frac{1}{Z} = \frac{1}{Z_1} + \frac{1}{Z_2}$ (e. g. R and C are in parallel, $Z = \frac{(R - j\omega CR^2)}{1 + R^2\omega^2C^2}$, Figure 1-6-B depicts the computer simulated Nyquist plot of this circuit.).

For a classic example of biomolecules immobilized at an electrode surface, the current flows through the working electrode, biomolecules, and electrolyte, and reaches counter electrode. Randles' circuit represents the equivalent circuit for this cell. To establish the circuit model for a cell and elucidate each component, EIS experimental data will be fit into model circuits by software such as ZSimpWin from Princeton Applied Research.[7]

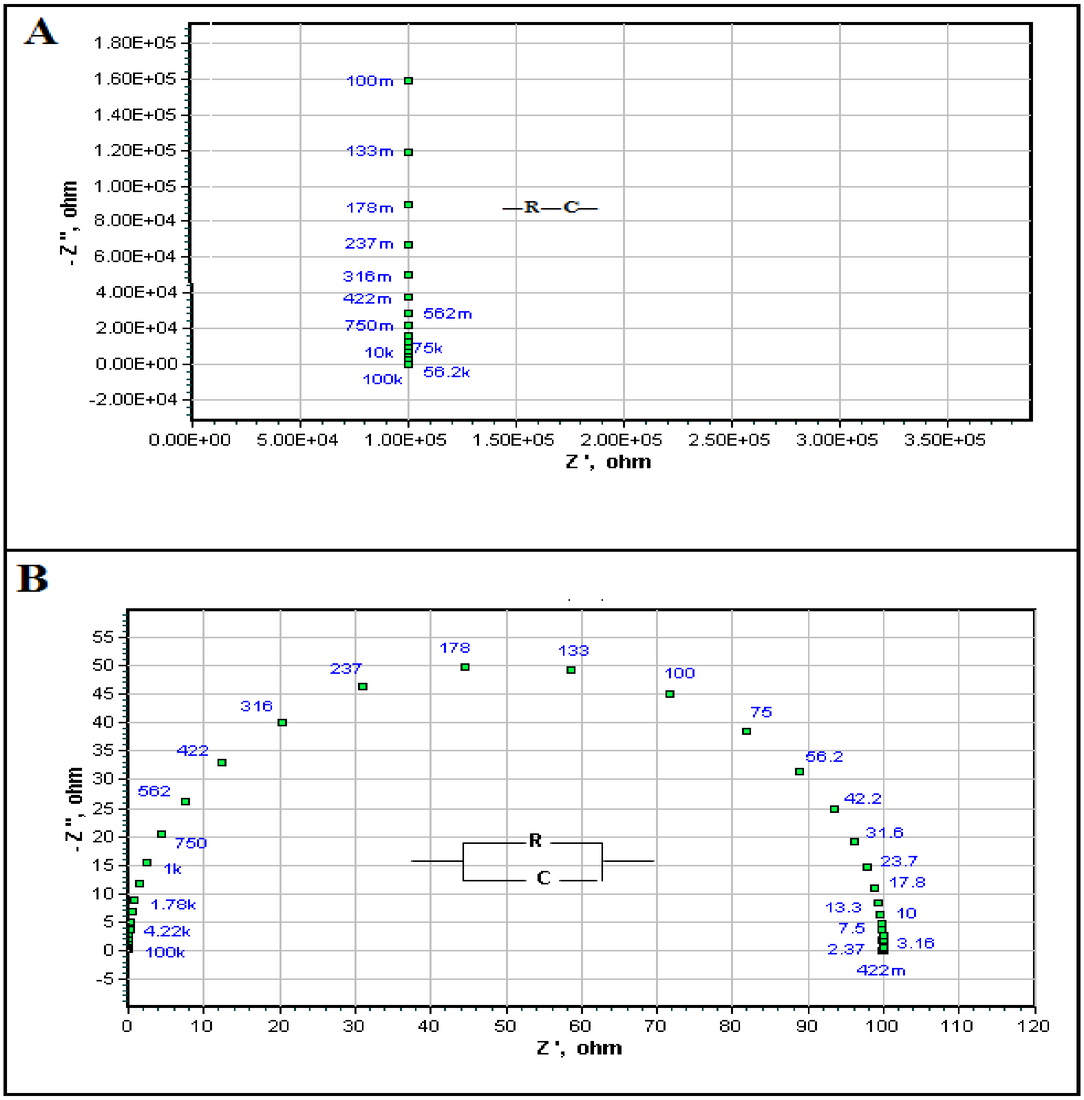

Figure 1-6 Computer simulations of EIS spectra of a circuit with resistor and capacitor in series (A), and a circuit with resistor and capacitor in parallel (B).

Chapter 2 - Experimental

2.1 DNA reorientation on glassy carbon surface driven by electric fields

All the fluorescence measurements were performed in Dr. Higgins' lab, with help from Dr. Higgins and Chenchen Cui. Electrochemical cells made of polydimethylsiloxane (PDMS) were fabricated by Dr. Jungkyu Kim in Dr. Bruce Gale's group at the University of Utah.

2.1.1 Materials

All reagents were used directly as obtained from Fisher Scientific. All solutions were made with deionized water (18.2 MΩ-cm resistivity) from a Millipore system. DNA oligonucleotides were purchased from the Midland Certified Reagent Company. Two different oligonucleotide probes and their complementary targets were utilized in this study: one with 34 bases (34-mer) and the other with 45 bases (45-mer). The probes and targets are listed as below:

P1: 5'-FAM6-AAGA AGAAGACAGCAAAGAGCAAGTCTTCTTCTT-Dabdt-3'Amino C7-3'

T1: 5'-AAGAAGAAGACTTGCTCTTTGCTGT CTTCTTCTT-3'

P2: 5'-FAM6-AAGAAGAAGAAGCAGCAAAGAGCAAGCCTTCTTCTTCTTCTT-Dabdt-3'Amino C7-3'

T2: 5'-AAGAAGAAGAAGAAGGCTTGCTCTTTGCTGCTTCTTCTTCTTCTT-5'.

The length of P1 is 11.92 nm and that of P2 is 15.55 nm.[64] And the structure of FAM6 is shown in Figure 2-1.

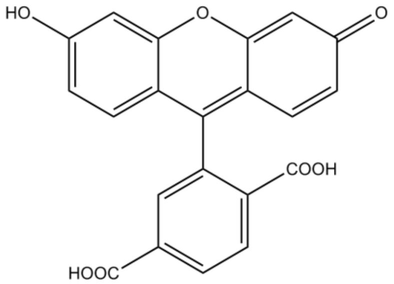

Figure 2-1 Structure of FAM 6

Phosphate buffered saline (PBS) with the normal concentration consisting of 137 mM NaCl, 2.7mM KCl, 8.1mM $Na_2HPO_4 \cdot H_2O$, and 1.76 mM KH_2PO_4 (i.e. 1X PBS) and the diluted solutions were employed to fix the pH at 7.4 for DNA functionalization and electrode passivation. Saline-sodium citrate buffer (0.3 M NaCl and 30 mM trisodium citrate, 2X SSC) was used for DNA hybridization. Tris-HCl buffer (tris(hydroxymethyl)aminomethane and HCl, pH=7.4, 10 mM) was used for electrochemical characterizations.

The hybridization temperature for 34-mer DNA was 75°C. For 45-mer DNA the hybridization temperature was around 85°C.

2.1.2 Preparation of DNA modified electrodes

2.1.2.1 Glassy carbon preconditioning

Glassy carbon plates (50 mm x 50 mm x 2 mm, width x length x height) purchased from SPi supplies were divided into small electrodes (around 17 mm x 15 mm x 2 mm, width x length x height). The glassy carbon electrodes were first rinsed with ethanol, polished with 0.05 µm gamma alumina slurry (Burhler) on napless polishing cloth for 5 min followed by washing and sonicating in deionized water for 15 min. In addition, the electrodes were electrochemically activated by etching in 1 M NaOH with one cycle of cyclic voltammetry (CV). The cyclic voltammogram was performed from -0.1 V to 1.2 V (vs. saturated calomel electrode, SCE), with scan rate 50 mV/s. Electrodes were rinsed with deionized water and stored in a petrish dish until used.

2.1.2.2 DNA functionalization

Glassy carbon electrodes were functionalized with DNA probes by incubating with 50 µL of 1 µM buffered DNA solution at 40 °C for 1 hour. The amino modified DNA was end grafted onto carboxylic groups on the glassy carbon surface in the presence of catalysts (25 mM 1-Ethyl-3-[3-dimethylaminopropyl]carbodiimide hydrochloride, 10 mM *N*-hydroxysulfosuccinimide in 1X PBS buffer).

2.1.2.3 Electrode passivation

After DNA probe funtionalization, the electrode was immersed in 1 mM hexylamine solution with the same catalyst conditions as in the functionalization step. Surface-tethered hexylamine served to passivate the remaining active sites on the glassy carbon surface.

2.1.2.4 DNA hybridization

Hybridization was performed by exposing the probe/hexylamine modified electrode to 5 µM target solution in 2X SSC buffer at 75 ^{o}C for 1 hour, after which it was cooled in the dark to room temperature.

Every step was followed by washing with 0.0067X PBS buffer and 20X SSC buffer. Electrodes with DNA were stored in 20X SSC buffer at 4 ^{o}C.

2.1.3 Instruments and experiment setup

2.1.3.1 Electrochemistry experiment

All the electrochemistry experiments were controlled by a potentiostat (CH Instrument 440A), and all the electrochemistry experiments were carried out in electrochemical cell with a typical three-electrode set up. Three types of electrochemical cells were employed for different experiments. The detailed set up will be listed later.

2.1.3.1.1 Electrochemistry employed in manipulating DNA switch

Electrochemical experiments were performed in a PDMS cell fabricated by the University of Utah (Figure 2-2) (4 mm x 0.2 mm, diameter x height), using a three electrode system (working electrode: glassy carbon; counter electrode: Platinum; quasi-reference electrode: Ag/AgCl), where the reference and counter electrodes were integrated “on-chip” in the PDMS cell. A square waveform of 10 steps (step width: 2 s) of alternating potentials was applied to the glassy carbon electrode. The potentials were switched between -0.2 V and +0.2 V with respect to open circuit potential (OCP). The OCP was measured in the PDMS cell and ranged from -0.09 to 0.11V vs. Ag/AgCl for different ionic concentrations.

2.1.3.1.2 Electrochemistry employed in measuring DNA density

To measure the DNA density on glassy carbon surface, all the electrochemistry experiments were performed in a Teflon cell (1.6 mL in volume) at room temperature. The working electrode was the glassy carbon electrode modified with a surface layer, and the electrode area was 0.071 cm^2. The Ag/AgCl (4M KCl) served as the reference electrode and the platinum wire coil served as the counter electrode. The electrolyte was purged with nitrogen for 5 minutes to remove oxygen. The electrode capacitance was determined in 10 mM tris-HCl buffer via CV by measuring the charging and discharging current. The DNA density was quantified via chronocoulometry (CC) by determining the charge of surface confined redox species-hexaammineruthenium (III) chloride. For CV, the scan rate was 100 mV/ sec; for CC, the potential was switched from +0.2 V to -0.3 V (or -0.35 V, depending on the electrodes' surface layers), and the measurement period was 4 seconds.

2.1.3.2 Wide field optical system setup

All optical measurements were performed on an inverted light microscope (Nikon Eclipse Ti). The sample was mounted on a sample stage above a 50X, 0.8 NA objective lens (Nikon, CF Plan), which was used both to deliver light to the sample surface for fluorescence excitation and for collection of fluorescence emitted from the sample. Laser light (488 nm) from a solid-state laser was used to excite fluorescence in the sample. Prior to incidence on the sample, the laser light was first passed through a diffuser, reflected from the surface of a dichroic beamsplitter (Q505LP), and focused into the back aperture of the microscope objective, producing an ~ 50 μm^2 illuminated region on the sample surface. The incident laser power was maintained at 500 µW, as measured just prior to the beamsplitter, in all experiments. Fluorescence collected from the sample passed back through the dichroic beamsplitter and was subsequently directed through a bandpass filter (Chroma HQ535/50 M) and a 515 nm longpass filter (CVI) prior to incidence on a thermoelectrically cooled electron multiplying CCD camera (Andor, iXon+) (Figure2-3). Fluorescence images were recorded at a rate of 8 frames or 20 frames per second, using an electron multiplying gain of 300 or 8, respectively. Later, the camera pixels were binded in units of 16 X 16 pixels.

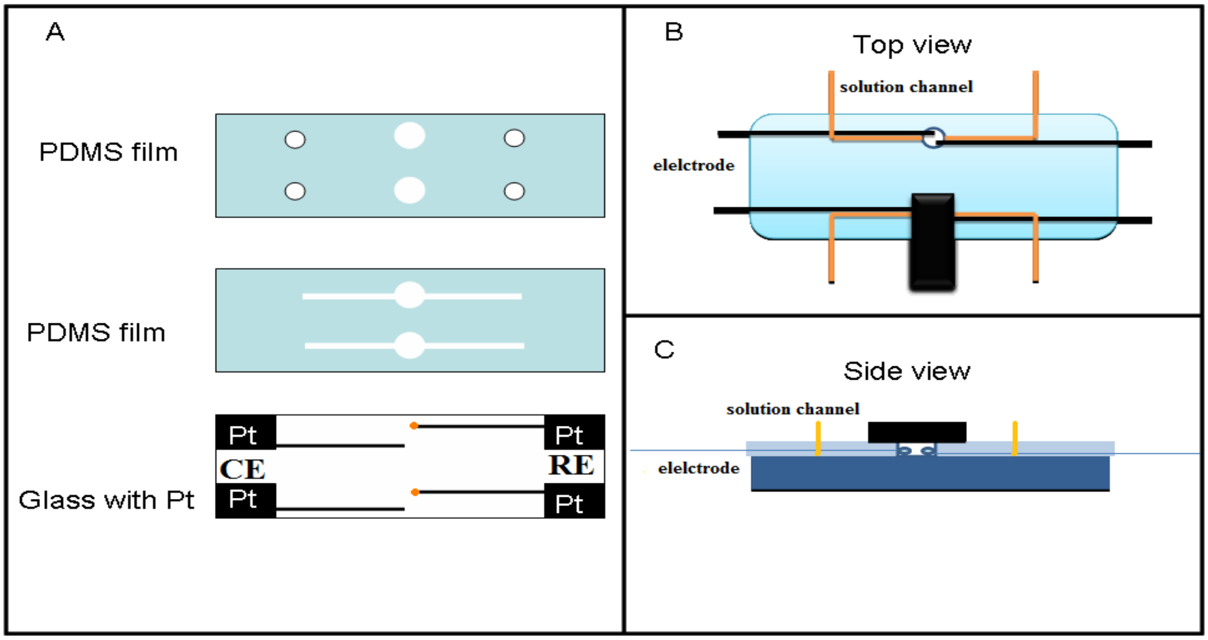

Figure 2-2 Schematic of the PDMS cell used in studies of DNA reorientation. A, three layers of the PDMS cell. In the bottom plot, the yellow dots indicate the quasireference electrode made of Ag/AgCl paste deposited on the Pt film. B, top view of the cell. C, side view of the cell.

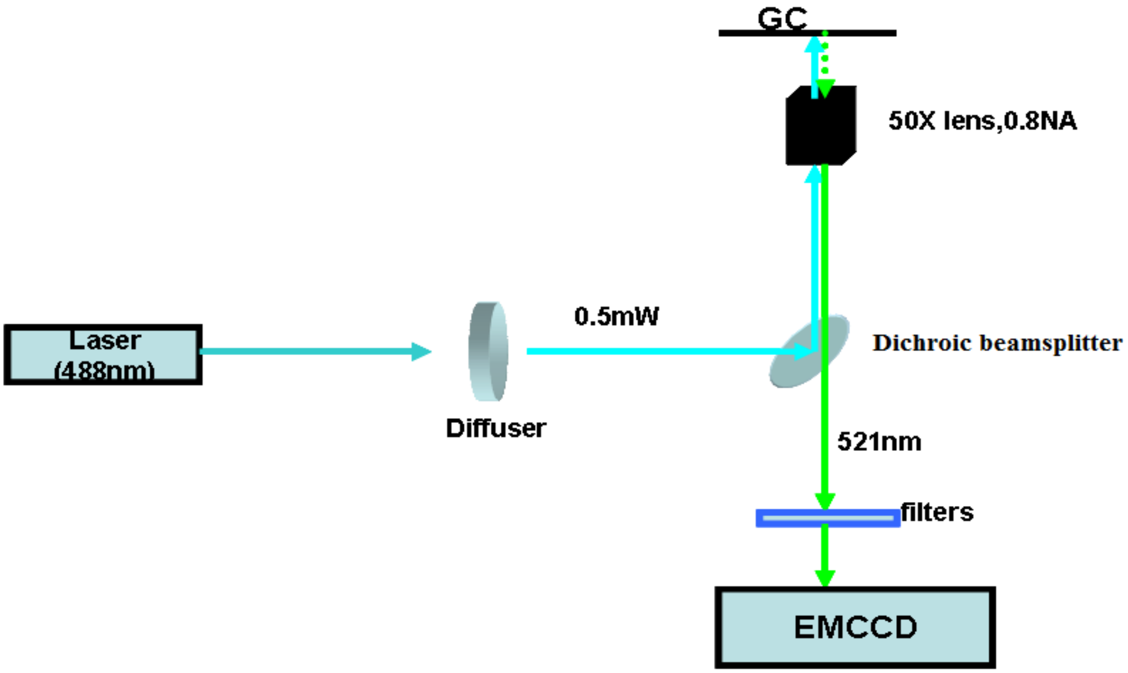

Figure 2-3. Light path of wide field optical system.

2.2 EIS detection of DNA hybridization

2.2.1 Materials

All the reagents were the same as those used in DNA reorientation in the glassy carbon project, except different probe (P_3) and target (T3) were employed.

P3: 5'-Cy3-AITTATCCCTCTCCATCAIICAIT-3'-AminoC7-3';

T_3: 5'-Cy5-<u>ACTGCCTGATGGAGAGGGATAACT</u>GGGGGGGGGG-3'.

2.2.2 DNA modified electrode preparation

We employed both glassy carbon and patterned CNF arrays for this study.

Modification of glassy carbon also included preconditioning, probe functionalization and target hybridization steps.

Modification of patterned CNF arrays used the same procedures as for glassy carbon. The preconditioning step was different from glassy carbon, and will be discussed in detail later in Chapter 3.

2.2.3 Instruments and experiment setups

A potentiostat (PARSTAT 2273, Princeton Applied Research Corporation) was used to perform impedance spectroscopy. We mainly tried normal EIS with AC amplitude 10 mV rms (for probing surface change), high AC potential EIS with AC amplitude 141 mV rms (for both probing the surface and driving the DNA movement), and REIS (real-time electrochemical impedance spectroscopy). Parameters such as AC amplitude, DC bias, and scanning frequency were varied as needed. Specific parameters listed in Chapter 3. The rms (root mean square) amplitude of the sinusoidal AC voltage is related to the peak amplitude that we discussed earlier as $\frac{V_0}{\sqrt{2}}$

The electrochemical cell for RIES measurements on glassy carbon electrodes was made of Teflon with a 3-electrode system. Glassy carbon served as the working electrode; platinum wire was used as the counter electrode; Ag/AgCl wire was used as the reference electrode. The cell volume was 160 μL.

The cell for patterned CNF arrays was fabricated by the University of Utah as will be shown in Chapter 3 together with the precondition procedures for the patterned CNF arrays. It was also a 3 electrodes system. CNF array served as the working electrode; a platinum wire was used as the counter electrode; SCE was used as the reference electrode.

2.3 Hairpin DNA melting and rehybridization driven by electric field

Fluorescence measurements of hairpin DNA dehyrbidization and rehybridization driven by electric fields on CNF arrays were mainly performed by Jeffrey Lange in Dr. Higgins' group. The major results have been discussed in Jeffrey's doctoral dissertation. Fluorescence measurements of hairpin DNA dehybridization and rehybridization on glassy carbon were finished with great help from Dr. Higgins. As-grown CNFs was produced by Dr. Jianwei Liu. Lateef Syed provided help for TEOS CVD and RIE procedure.

2.3.1 Materials

All reagents were the same as those used in the project for DNA reorientation on glassy carbon. Hairpin DNA was designed with an 11-mer stem and a 12-mer loop.
5'-FAM6-<u>AAGA AGAAGAC</u>AGCAAAGAGCAA<u>GTCTTCTTCTT</u>-Dabdt-3'Amino C7-3'

2.3.2 Instruments and experiment setup

The same PDMS cell fabricated by the Univerisity of Utah as used in DNA reorientation project was employed here. A potentiostat (CH Instrument 440A) was used here to control potential bias.

2.3.3 VACNF chip fabrication

Chip fabrication usually followed the following procedure:

First, a 50 nm thick chromium layer was coated on the clean silicon substrate. On top of the chromium layer, a 22.5 nm nickel was deposited as the catalyst for growing CNFs.

Second, the growth of CNFs was performed by PECVD. The nickel catalyst was heated to 500 ^{o}C so that it would be broken into randomly distributed Ni nanoparticles. During CNFs growth, the C_2H_2 was reduced to form the CNF in an NH_3 atmosphere at 800 ^{o}C for 15 minutes. The CNFs produced in this manner were usually 50-100 nm in diameter and ~5 μm in length.

Third, the as-grown VACNF chip was place in the CVD chamber for SiO_2 encapsulation. TEOS pressure was maintained at 400 mTorr for 6 to 7 hours at 730 ^{o}C.

Fourth, 0.05 um alumina slurry was used to planarize the SiO_2 surface. RIE was subsequently used to etch away the SiO_2. The plasma generated by O_2 and CHF_3 in the RIE vacuum chamber etches away SiO_2 and expose the CNF tip. The etching time may be varied to control the density of exposed CNF.

Fifth, before being attached with DNA, the chip was treated with HNO_3 and NaOH to remove the polymer formed in the last step so that there will be enough carboxylic groups for DNA modification.

Chapter 3 - Results and discussion

3.1 DNA reorientation on glassy carbon surfaces driven by an electric field

3.1.1Fluorescence detection of DNA reorientation dynamics

As described in Rant's paper[19], dsDNA can be manipulated by an electric field. Here, we observed the similar electric field effect on driving DNA reorientation. In our platform, the 5' end of dsDNA was labeled with FAM6, and the dsDNA was linked to the glassy carbon surface at the 3' end. A 488 nm green laser was used to excite FAM6, and the emission photons around 520 nm were detected by a thermoelectrically cooled CCD camera. As shown in Figure 3-1-A, the fluorescence signal alternates "up and down" periodically in phase with the applied potential steps. The higher fluorescence intensity level correlates with the negative potential (-0.2 V vs. OCP), which repels the DNA from the electrode. The lower fluorescence intensity level corresponds to positive potential (+0.2 V vs. OCP), which attracts the DNA to the electrode. Previously published theories for energy transfer between the dye and electrode theory can be used to explain the potential dependent switching of the fluorescence signal. The fluorescence is quenched through energy transfer as the separation between dye and electrode becomes smaller under the influence of a positive potential. Likewise, at negative potential, the fluorescence increases as there is less energy transfer when the dye and electrode ~~is~~ are separated According to Rant's research, reorientation finishes within 0.001 seconds, which is beyond the temporal resolution of our setup.

In addition to the changes in fluorescence signal due to potential dependent reorientation of DNA (see Figure 3-1-A), the detected signal also exhibits a drifting background, as depicted by the dark image data shown in Figure 3-1-B. The background drift was attributed to the settling of electron multiplying gain of the CCD camera. The background drift could be eliminated either mathematically or experimentally. Mathematically, we could fit the background to an exponential function (Figure 3-1-C) and subtract the fitting data from the raw data (Figure 3-1-D). Experimentally, we could start applying potential step after the CCD camera is stabilized. As shown in Figure 3-2, the CCD camera is turned on first, after around 5 seconds, the laser shutter is opened, which leads to the sudden increase in fluorescence signal; 10 seconds later, the potential steps are applied.

Besides the fast initial switching of the fluorescence signal, a slow signal decay on a 0.1-1 second timescale is also observed (see Figure 3-3-A). As discussed in the introduction RET is inversely proportional to the 3rd or 4th power of the distance between the fluorophore and metallic surface if other parameters are the same. Thus, the fluorescence signal decay after the initial switching indicates that the relative position of FAM6 to glassy carbon surface continues to change. Figure3-3-B presents a model for this phenomenon. As dsDNA anchored on glassy carbon surface at 3' end, it would first stay at a position (position 1) which is determined by the equilibrium between electrostatic interactions and Brownian motion. The dsDNA is driven to stand up abruptly (to position 2) by electrostatic interaction between the negative charges on DNA and the negative potential bias. After this, dsDNA starts to "relax" by tilting (from position 2 to position 3) close to energy minimum position 1, which may be associated with the weakened electrostatic interaction due to rearrangement of the EDL. When a positive potential step occurs, the dsDNA position quickly switches from position 3 to position 4 due to the attractive electrostatic interaction. Then the dsDNA again "relaxes" by tilting to position 5 close to position 1. It is quite straight forward to explain fluorescence signal during the dsDNA switching from position 1 to position 2, similar to Rant's reports. But the slow relaxation part is an interesting new phenomenon not shown in any of Rant's data. The following discussion will provide more analysis, and a more detailed model to explain the experiment data.

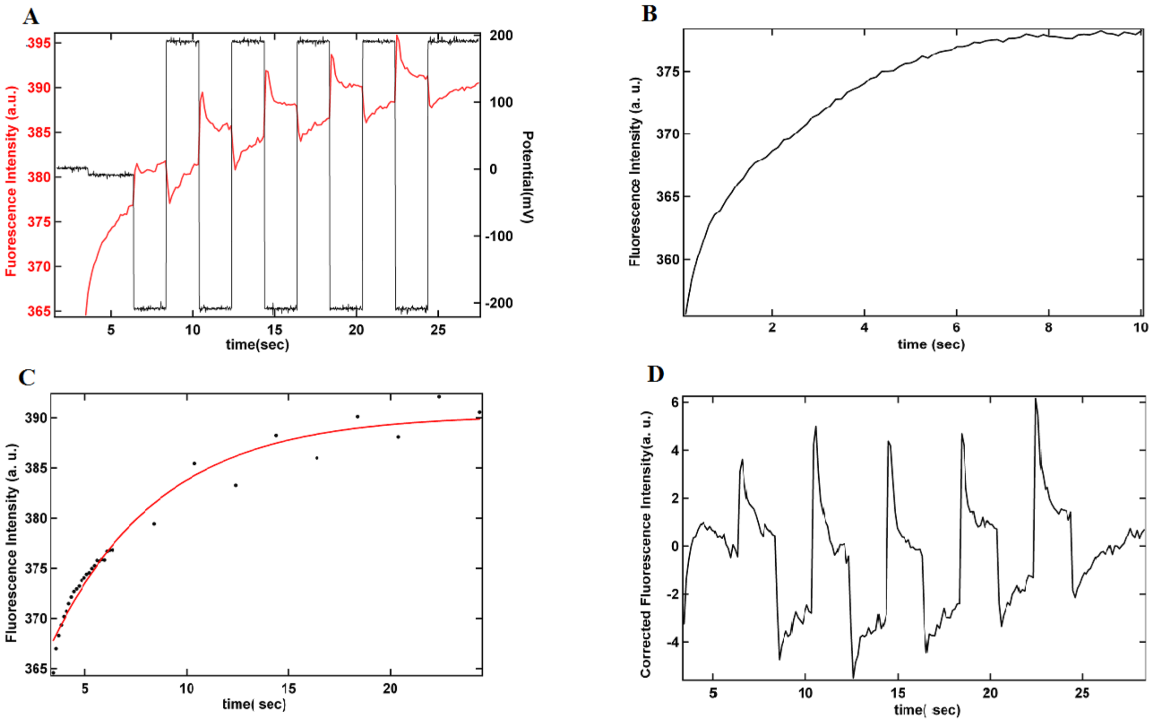

Figure 3-1. Electrical switching of dsDNA layer end-grafted to a glass carbon surface. (*A*) The fluorescence signal emitted from FAM-6 labeled dsDNA layer (red line) during application of a square wave potential (black line) between -0.2V (vs. OCP) and +0.2V(vs. OCP). (*B*) Background signal of the system, collected without applying laser and potential. (*C*) Exponential fitting of data points between 3.454 s and 6.33 s in (*A*) and the average value of intensity when switching the potential. (*D*) The corrected fluorescence signal by subtracting (*C*) from (*A*).

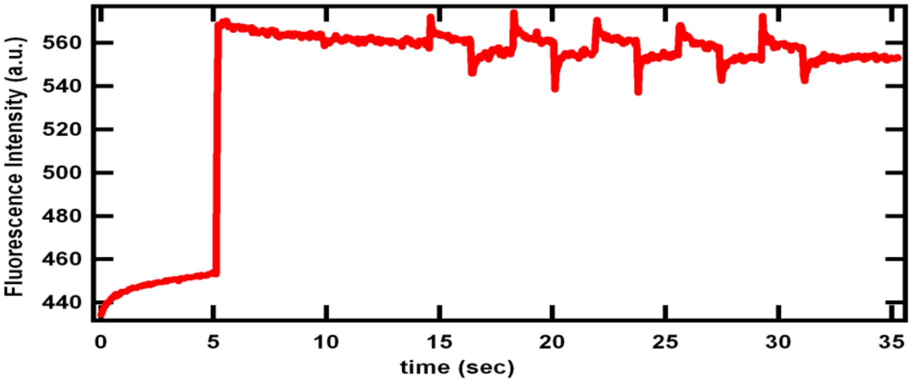

Figure 3-2. Raw data by experimentally eliminating the drifting background. 0-5 seconds, CCD camera on, shutter off, potential bias off; at 5 seconds, CCD on, shutter on, potential bias off; 15 second, CCD on, shutter on, potential bias on.

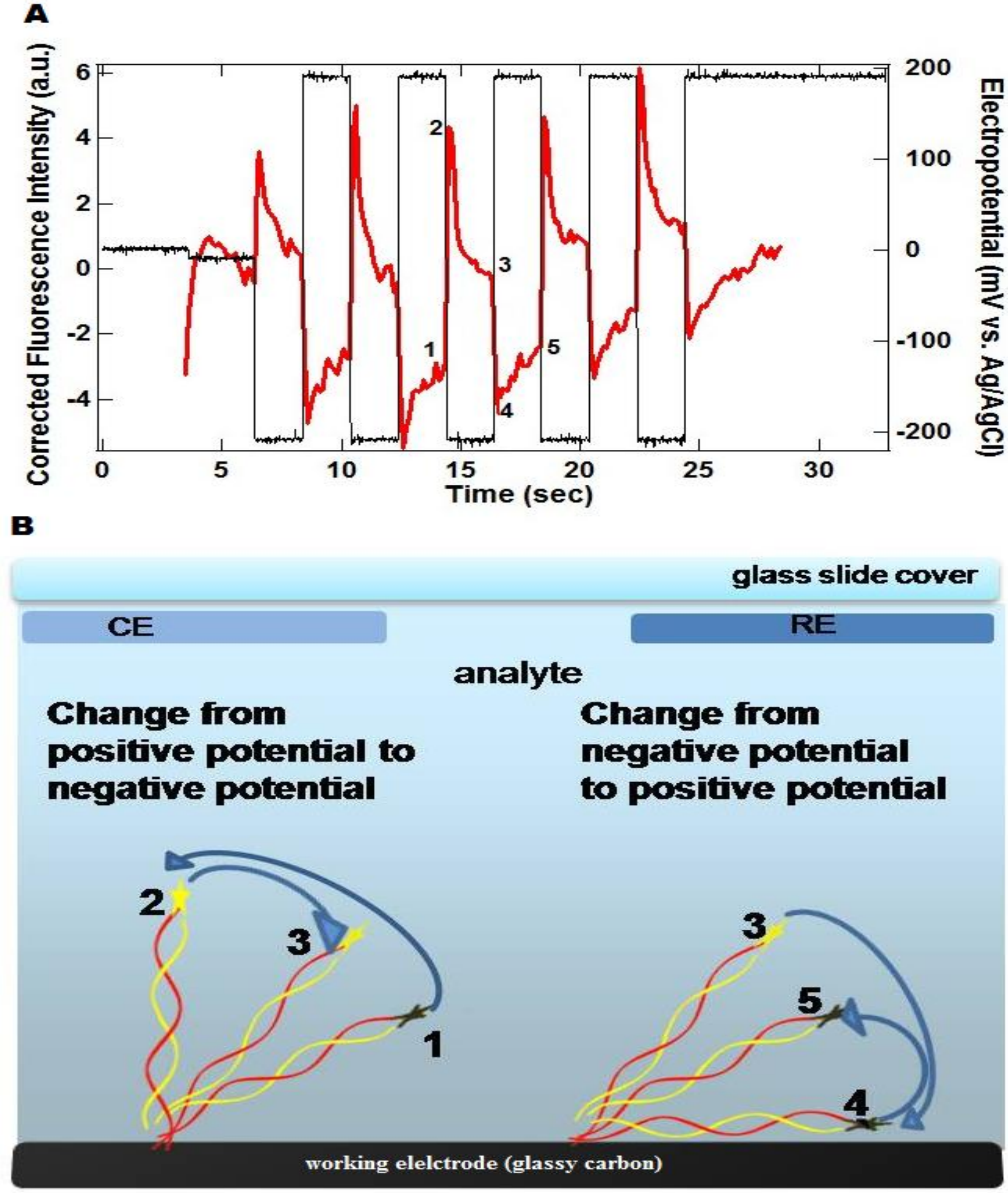

Figure 3-3 A. Fluorescence response (thick red line) to the applied potential steps (thin black line). B. A simple model of DNA switching and reorientation driven by electric field. Glassy carbon electrodes (WE, working electrode) modified with 34-mer dsDNA are attached to the PDMS cell with fluidic channels filled with PBS buffers. Potentials steps are applied to WE with respect to RE (Ag/AgCl).

3.1.2 Ionic strength effects on the dynamics of DNA reorientation

3.1.2.1 Fluorescence detection of DNA reorientation at different ionic strengths

As mentioned in Rant's research, the electric field generated by the applied bias decays to near zero beyond the Debye length due to the formation of the EDL. The electric field strength within the EDL is very strong at kV/cm scale. It is this strong electric field that modulates the fast switching of DNA. For the slow dynamics of dsDNA reorientation after the quick switching, we believe that it may be due to the EDL redistribution after the double layer charging process. The EDL thickness is directly related to the ionic strength, so we suspect that the dynamics of DNA reorientation will vary with the ionic strength. To confirm this hypothesis, we studied the dynamics of 34-mer dsDNA reorientation at 4 different ionic strengths by varying the concentration of PBS buffer (Figure 3-4); and as a supplementary, we also studied the dynamics of 45-mer dsDNA reorientation at 3 different ionic strengths (Figure 3-5).

The composition of 1X PBS buffer is 137 mM NaCl, 2.7mM KCl, 8.1mM $Na_2HPO_4 \cdot H_2O$, and 1.76 mM KH_2PO_4. The PBS buffer helps to maintain the pH around 7.4. Here we use diluted 0.0067 X, 0.02 X, 0.067 X and 0.2 X PBS buffer. The corresponding double layer thickness was 10 nm, 5.8 nm, 3.2 nm, and 1.8 nm.

Despite the ionic strength and DNA length variation, the fluorescence data reflects that the DNAs behave in a similar fashion. An abrupt increase/decrease in fluorescence signal is observed right after the potential step, followed by a slow recovery.

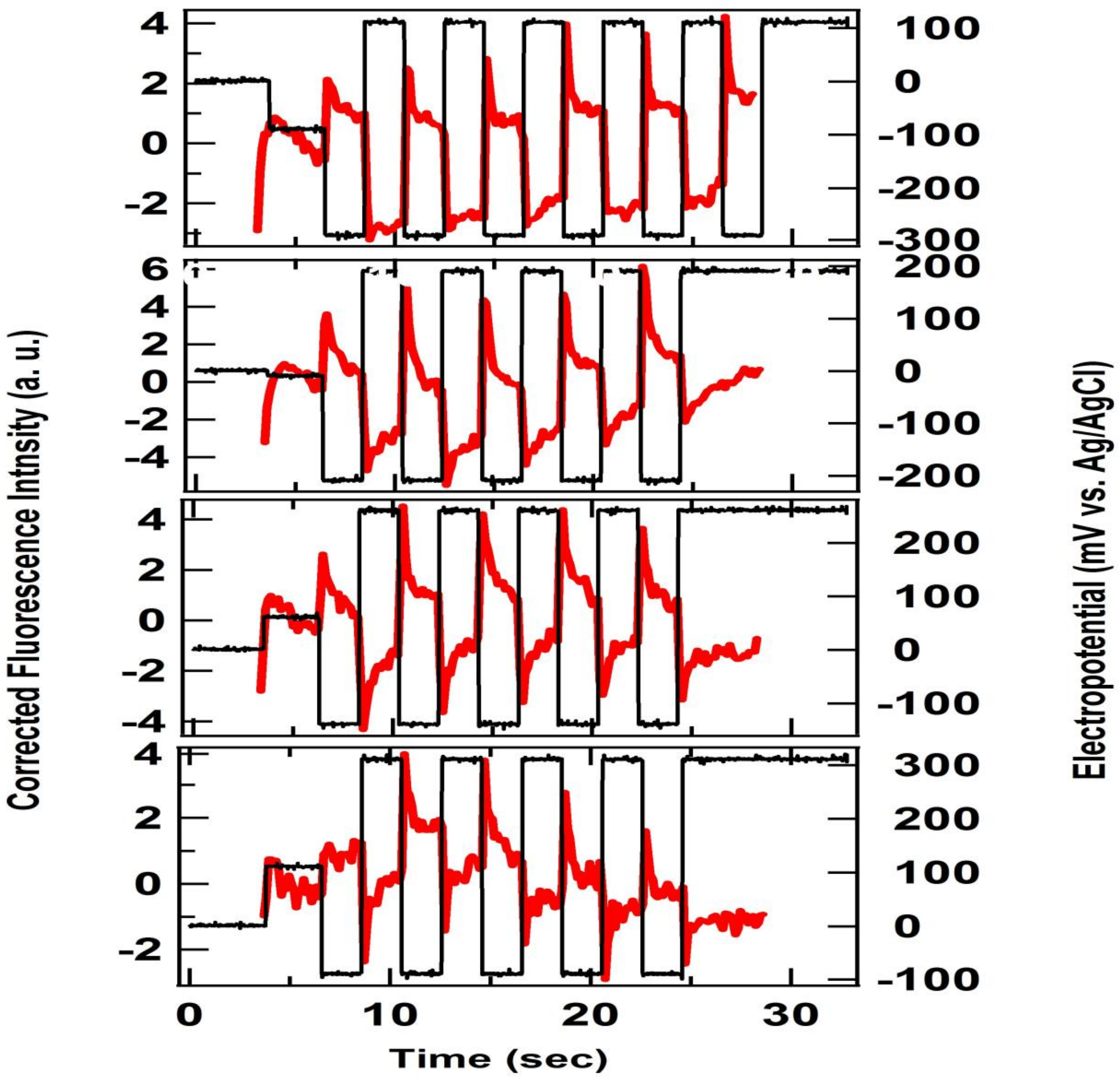

Figure 3-4 The fluorescence modulation of 34-mer dsDNA at four different buffer concentrations. From top to bottom, buffers are 0.0067X, 0.02X, 0.067X and 0.2X PBS.

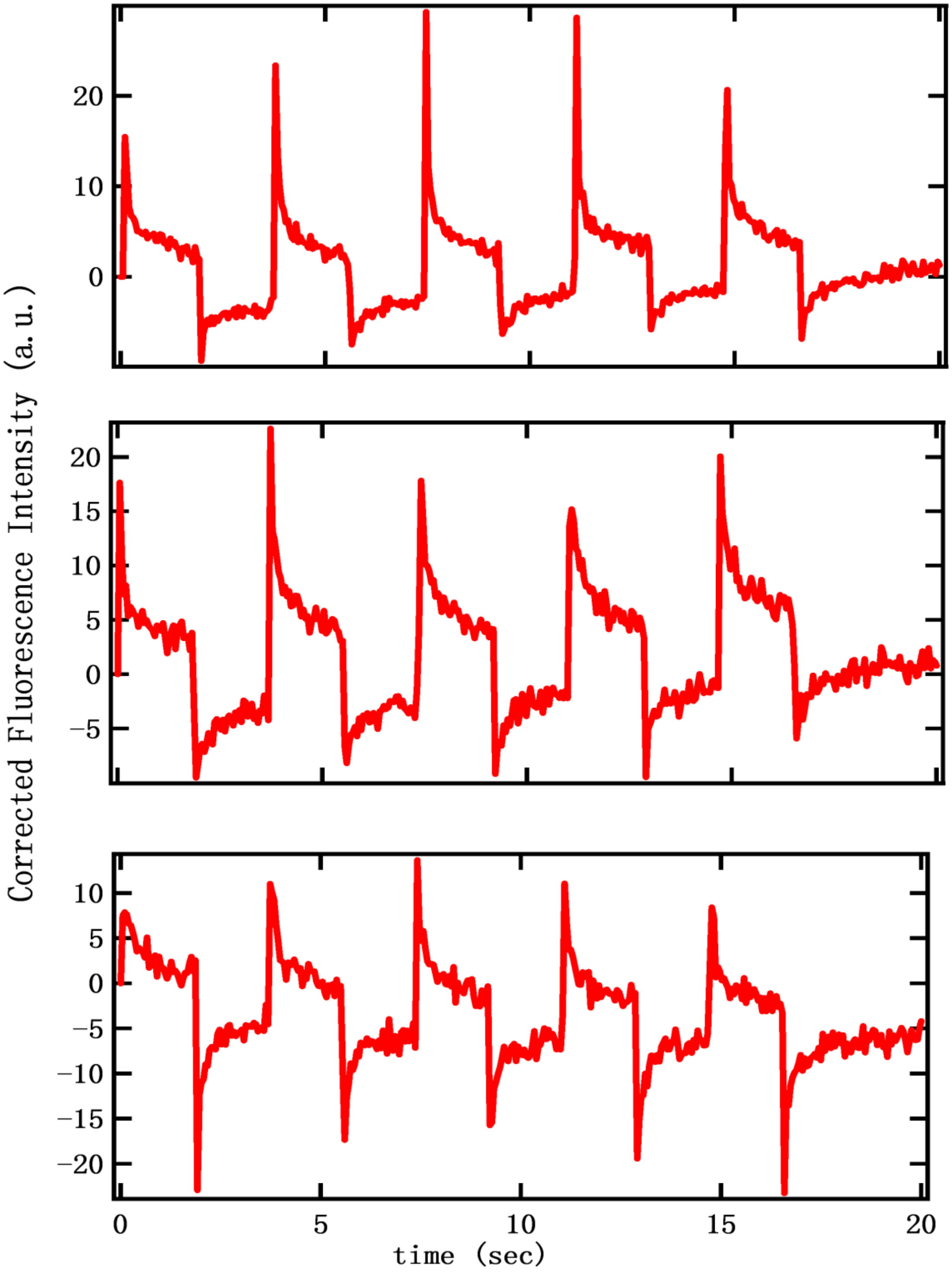

Figure 3-5 The fluorescence modulation of 45-mer dsDNA at four different buffer concentrations. From top to bottom, buffers are 0.02X, 0.067X and 0.2X PBS.

3.1.2.2 Electric field driven DNA switching at different ionic concentrations

For all DNA reorientation studies, the electric field driven DNA switching effect can be described by the peak-to-peak change in fluorescence (ΔF) between position 2 and position 4 in Figure 3-3-B. These data are plotted in Figure 3-6 (for 34-mer dsDNA) and Figure 3-7 (for 45-mer dsDNA). For both DNA lengths, the fluorescence change driven by the applied potential decreases as the buffer concentration increases from 0.02X to 0.2X PBS buffer, which is in agreement with Rant's data.

Rant's research result indicates that the modulations of dsDNA by an electric field are the same for ionic concentrations that are smaller than 6 mM. But for ionic concentration larger than 6 mM, the modulation effect decreases as the concentration increases. They claimed that the electrostatic torque generated by the EDL acting on the rigid dsDNA rod was reduced as the ionic concentration increased.

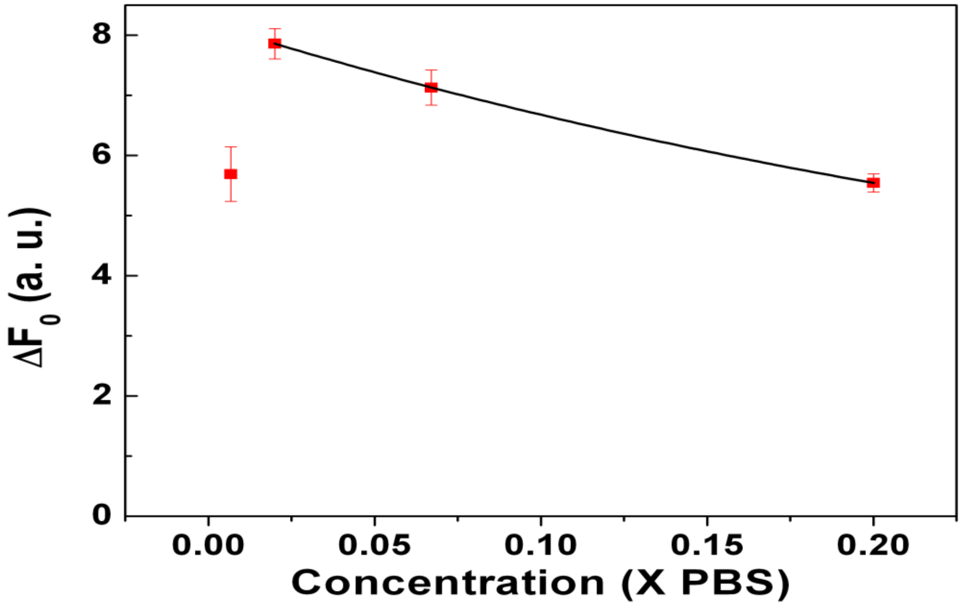

Figure 3-6. The change in fluorescence signal between position 2 and position 4 vs. concentration for 34-mer dsDNA.

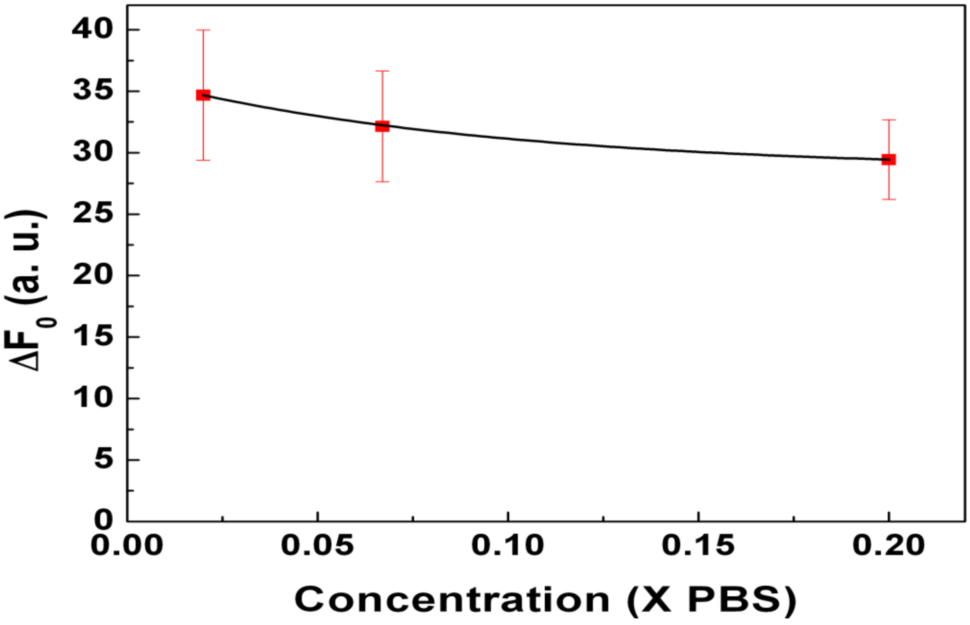

Figure 3-7. The change in fluorescence signal between position 2 and position 4 vs. concentration for 45-mer dsDNA.

3.1.2.3 Quantitative correlation between the fluorescence intensity and the tilt angle of dsDNA

In order to obtain the DNA tilt angle, we did the following analysis based on the fluorescence signal we obtained from 34-mer and 45-mer dsDNAs

When the excitation laser illuminates a fluorophore, the fluorophore will be promoted to an excited state. The molecule does not stay in the excited state for long as it will quickly lose energy in the form of heat or photons, or it will transfer the energy to a quencher. These processes can be described as follows: [16]

Excitation: $A + h\upsilon \rightarrow A^*$ $\qquad rate = k_{ex} \times [A]$ **(3.1)**

Emission: $A^* \rightarrow A + h\upsilon'$ $\qquad rate = k_{em} \times [A^*]$ **(3.2)**

Energy transfer to quencher: $A^* + Q \rightarrow A + Q^*$ $\qquad rate = k_{et} \times [A^*][Q]$ **(3.3)**

Deactivation: $A^* \rightarrow A + heat$ $\qquad rate = k_d \times [A^*]$ **(3.4)**

Here, A is the fluorophore in the ground state, A^* is the fluorophore in the excited state, Q is the quencher in the ground state, and Q^* is the quencher in the excited state. The k parameters are the rate constants for each process.

As the system reaches a steady state, the rate of formation of A^* should equal the rate of its decay.

$$k_{ex}[A] = k_{em}[A^*] + k_{et}[A^*][Q] + k_d[A^*] \qquad \textbf{(3.5)}$$

In our case, the energy transfer was between fluorophore and the glassy carbon surface, so $[Q]$ is 1.

$$k_{ex}[A] = k_{em}[A^*] + k_{et}[A^*] + k_d[A^*] \qquad \textbf{(3.6)}$$

The quantum yield of emission with energy transfer is

$$\phi_{em} = \frac{k_{em}[A^*]}{k_{ex}[A]} = \frac{k_{em}}{k_{em} + k_{et} + k_d} \qquad \textbf{(3.7)}$$

The quantum yield of energy transfer is:

$$\phi_{et} = \frac{k_{et}[A^*]}{k_{ex}[A]} = \frac{k_{et}}{k_{em} + k_{et} + k_d} \qquad \textbf{(3.8)}$$

The quantum yield of emission without energy transfer is

$$\phi_0 = \frac{k_{em}}{k_{em} + k_d} \tag{3.9}$$

Thus we can write:

$$\phi_{et} = 1 - \frac{\phi_{em}}{\phi_0} \tag{3.10}$$

According to dipole-surface energy transfer theories, for a fluorophore that is close to a metallic surface, the energy transfer efficiency is found to be inversely proportional to the fourth power of the distance (d) between fluorophore and metallic surface:[27, 28]

$$\phi_{et} = \frac{1}{1 + \left(\frac{d}{d_0}\right)^4} \tag{3.11}$$

d_0 is the distance where 50% energy transfers to the quencher.

Combining (3.10) and (3.11):

$$\frac{\phi_{em}}{\phi_0} = 1 - \frac{1}{1 + \left(\frac{d}{d_0}\right)^4} \tag{3.12}$$

Since the relationship between quantum yield and fluorescence intensity (I) is linear, we can get equation 3.13 which is a function of d_{34}, d_{45}, and d_0, with the subscripts on the former two indicating the number of base pairs of dsDNAs:

$$\frac{\phi_{34}}{\phi_{45}} = \frac{I_{34}}{I_{45}} \tag{3.13}$$

As a reminder, we used different parameters which may affect the absolute value of fluorescence intensity when we recorded the fluorescence signal. The parameters for data acquisition determine that the absolute signal of 45-mer dsDNA is amplified by 3.2096 times comparing to that of 34-mer dsDNA (Table 3-1). In all these experiments, we maintained the same laser power at 0.5 mW ± 1% and the same laser alignment and illuminated area. We assume that the variation of the density of dsDNA on each chip is quite small and could be ignored in our calculation.

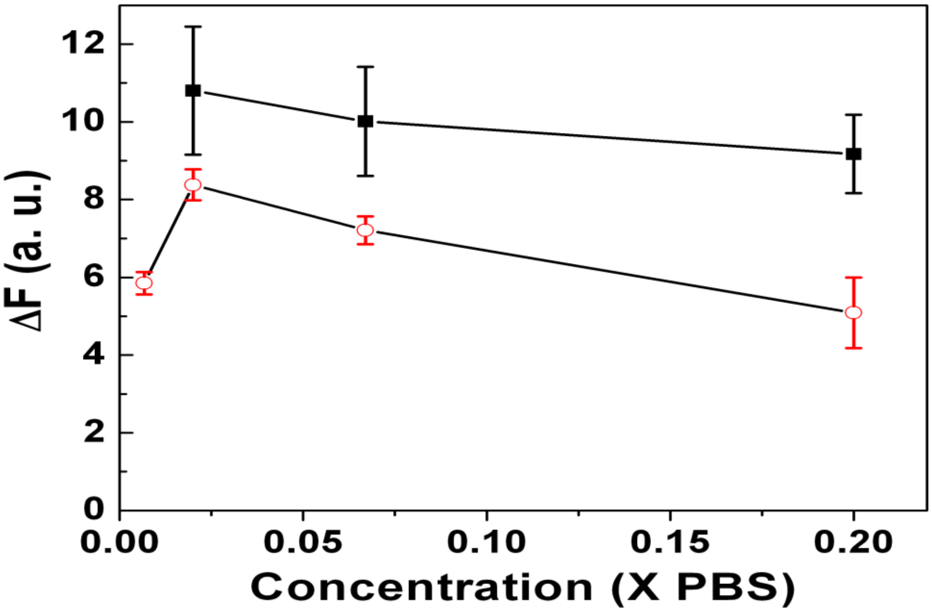

Figure 3-8 The corrected ΔF (in arbitrary units) between position 2 and 4 vs. PBS concentration for 45-mer dsDNA (black square) and 34-mer dsDNA (red circle). ΔF is the average value from least 3 potential steps after subtracting the background. The value of ΔF has been normalized by the amplification factors due to the detector setting (as listed in Table 3-1).

Table 3-1 Detector setting parameters in wide field fluorescence measurements.

	Bining(pixel X pixel)	Electron multiple gain	Exposure time (sec)	Amplification factor
34-mer dsDNA	1 X 1	300	0.1072	1
45-mer dsDNA	16 X 16	8	0.0504	3.2096

Assuming that when dsDNA is at position 4 (i.e. lying down on the electrode surface (Figure 3-3 B)), the distance between FAM6 and the glassy carbon surface is quite small, the energy transfer efficiency (ϕ_{et}) is close to 100%, and that, at position 2, dsDNA is fully extended, ΔF between position 2 and position 4 could be correlated to represent the distance between FAM6 and glassy carbon surface, which should be the length of dsDNA plus the length of the 7 carbon linker (with bond length 0.15 nm, bond angle 109.5^{o}). So the length of 34-mer dsDNA (d_{34}) that we used is around 11.92 nm, and the length of 45-mer dsDNA (d_{45}) is 15.55 nm.[64] In addition we know that

$$\Delta F_{34} = 8.38;\ \Delta F_{45} = \frac{34.67}{3.210} = 10.80 \text{ (Figure 3-8)}$$

Inputting these into equations 3.12 and 3.13, we derive that d_0 is 11 nm from our experimental data.

Theoretically, d_0 can be determined by an equation given by Strouse (equation 3.14), which is based on a model described by Persson. A value of 8.5 nm is obtained [27, 28]

$$d_0 = (0.225 \times \frac{c^3 \phi_{FAM6}}{\omega_{FAM6}^2 \omega_F \kappa_F})^{\frac{1}{4}} \qquad \textbf{(3.14)}$$

where c is the speed of light (3 x 10^8 m/s); ϕ_{FAM6} is the quantum yield without energy transfer to the electrode surface (0.8); ω_{FAM6} is the angular frequency of dye (3.8 x 10^{15} s^{-1}); ω_F is the Fermi angular frequency of glassy carbon (7.0 x 10^{15} s^{-1}) and κ_F is the Fermi wave vector of glassy carbon (1.1 x $10^{10}$$m^{-1}$). These two parameters could be deduced from the Fermi energy of glassy carbon (E_F =4.6 eV or 7.4 x 10^{-19} J):

$$\omega_F = \frac{E_F}{\hbar} \qquad \textbf{(3.15)}$$

$$\kappa_F = \frac{\sqrt{2mE_F}}{\hbar} \qquad \textbf{(3.16)}$$

where $\hbar$ is the reduced Planck constant (6.58 x 10^{-16} ev • s or 1.05 x 10^{-34} J • s); and m is the mass of an electron: 9.11 x 10^{-31} kg.

Our experimentally derived value of d_0 (10.95 nm) is slightly higher than the theoretical d_0 (8.5 nm). Three factors may account for this result: (1) The experimental derivation of d_0 is based on the assumption that dsDNA is fully extended at position 4 in 0.02 X PBS when applying -0.2 V vs.OCP potential; (2) the Strouse equation was originally derived for dye-nanoparticle system. For metal nanoparticles, the probability of energy transfer is enhanced since there is much stronger electric field due to the surface plasma resonance; and (3) The glassy carbon electrode may have very different properties from the metal electrodes.

In any case, our model and experimental results provide a useful method to derive the tilt angle of dsDNAs at different positions from the change in fluorescence intensity at any position comparing to position 4.Table 3-2 is one example of the tilt angles for position 1, 3, 5 for 45-mer dsDNA in 0.02X PBS buffer. Interestingly, the tilt angles for positions 1 and 5 are about the same, indicating that dsDNA will relax to a common equilibrium position if given enough time after each potential step. Table 3-3 and table 3-4 show the tilt angle at position 1 and 5 for different ionic concentrations for 45-mer dsDNA and 34-mer dsDNA. The correlation between the characteristic positions in the fluorescence spectra and the tilt angle was schematically illustrated in Figure 3-3.

Table 3-2 Example of tilt angles at position 1, 3, 5 for 45-mer dsDNA in 0.02X PBS buffer.

	Position 1	Position 3	Position 5
ΔF(n,4)	1.5±0.3	3.8±0.4	1.5±0.4
Tilt angle (degree)	25±2	34±3	25±3

Table 3-3 Tilt angle at position 1 and 5 of 45-mer dsDNA in different ionic strength.

	Position 1 (tilt angle, degree)	Position 5 (tilt angle, degree)
0.02 XPBS	25±2	25±3
0.067XPBS	27±3	30±3
0.2X PBS	35±4	34±4

Table 3-4 Tilt angle at position 1 and 5 of 34-mer dsDNA in different ionic strength

	Position 1 (tilt angle, degree)	Position 5 (tilt angle, degree)
0.0067X PBS	15±3	19±5
0.02XPBS	23±2	27±1
0.067XPBS	28±1	27±2
0.2XPBS	28±2	26±3

3.1.2.3 Analysis of the kinetics of DNA reorientation

By a closer look at the fluorescence spectra, the decay of the fluorescence signal could be fit with an exponential curve:

$$F = F_0 + A * \exp\left(\frac{t - t_0}{\tau}\right) \tag{3.17}$$

where τ is the decay time constant related to the DNA reorientation rate. A smaller τ indicates a faster reorientation.

Figure 3-9 is one example showing the original data and the fitting results at two ionic concentrations. Only the data in one potential cycle is shown, a potential step to -0.2V vs. OCP at zero time followed by a step to +0.2 V vs OCP at 2.0 second. First, it depicts that the decay constants varied with the ionic concentration which agrees with our hypothesis. Second, the trend in how the decay constant varies at the negative potential is different from that at the positive potential.

Figure 3-10 shows the summary of τ of DNA reorientation at positive/ negative potential steps of 34-mer dsDNA on glassy carbon electrodes. Figure 3-11 shows the similar results for 45-mer dsDNA. Clearly, the decay constants change with the concentration and show the opposite trend according to the potential bias direction. For positive potential, the DNA reorientation time constant decreases as the ionic strength increases. Oppositely, for the negative potential, the DNA reorientation time constant increases as the ionic strength increases.

For 34-mer dsDNA, the decay constant of positive potential step decreases from 1.8 to 0.3 second as ionic strength increases from 0.02 X to 0.2 X PBS; while for negative potential step, it increases from 0.16 to 0.38 second. Generally, the fluorescence signal decays slower at positive potential step than at the negative potential step when low ionic strength is used. This phenomenon was also observed with the 45-mer dsDNA.

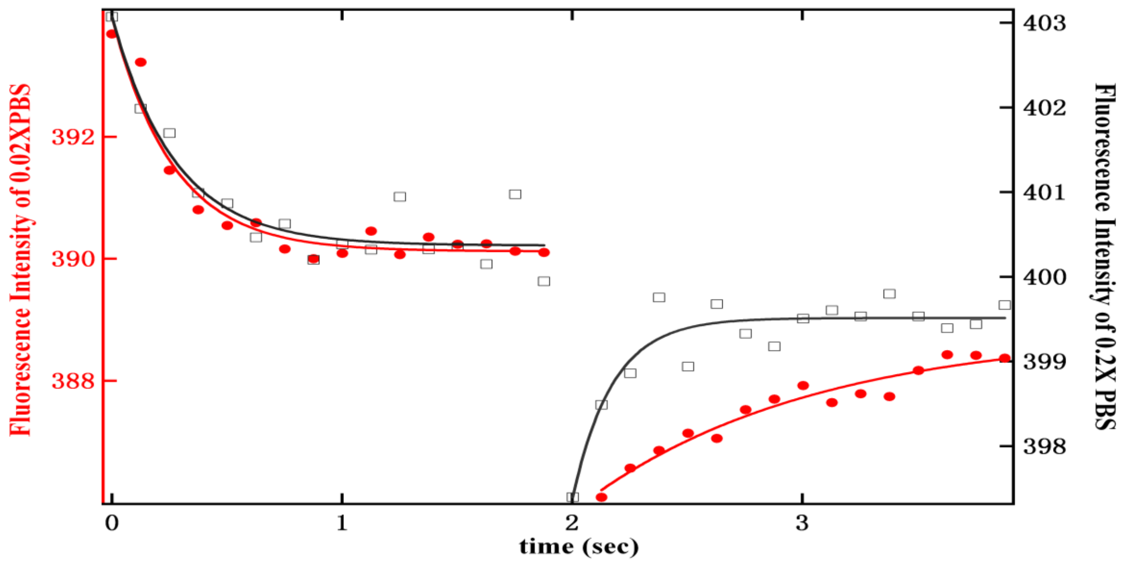

Figure 3-9. Fluorescence signal vs. time after potential steps of 34-mer dsDNA. Black open squares are fluorescence signal at 0.2X PBS and red solid circles are fluorescence signal at 0.02X PBS. Left upper part is under a negative potential step; right lower part is under a positive potential step. Black and red lines are the exponential fitting curves.

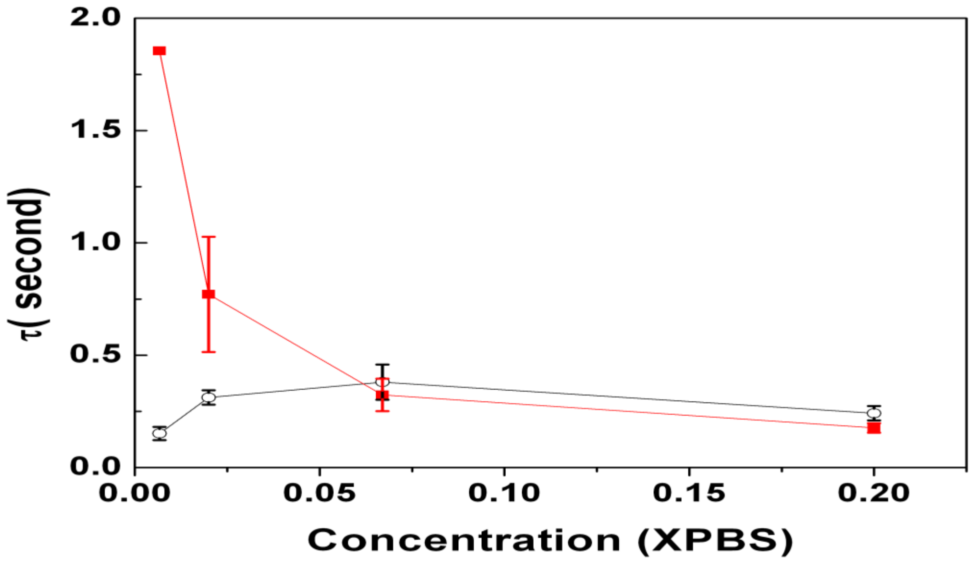

Figure 3-10 The reoreintation time constant vs. concentration at positive and negative potential steps for 34-mer dsDNA. Red squares depict the decay constant at positive potential step; black circles show the decay constant after negative potential step.

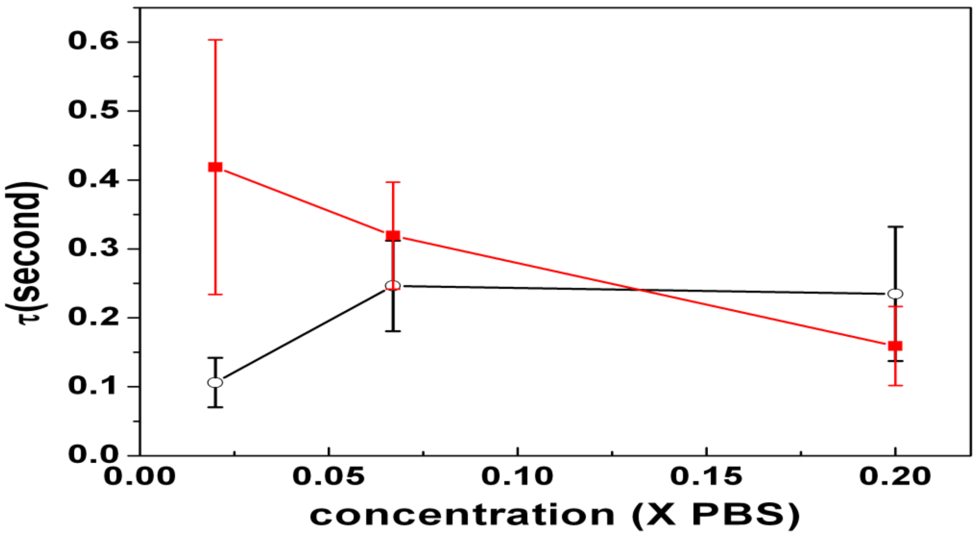

Figure 3-11. The reoreintation time constant vs. concentration at positive and negative potential steps for 34-mer dsDNA. Red squares depict the decay constant at positive potential step; black circles show the decay constant after negative potential step.

3.1.3 Transition time constant for DNA reorientation and the electric double layer charging

By studying the time-resolved response of 48-mer dsDNA to the 300Hz alternating potential, Rant et al. have demonstrated that the transient time of quick DNA switch is correlated to the "build up" EDL—time required to charge EDL. Both of them finished within 100 µs.

We also recorded the current response simultaneously with the fluorescence response as the potential step was applied (Figure 3-12) to see whether there is a correlation between these two. The fitting shows that the time constant of the current decay is 0.01s, while the time constant of fluorescence signal decay is at minimum of 0.1s. The time constant of current decay could be determined by measuring the solution resistance and the double layer capacitance ($\tau = R \bullet C$). From our previous study, the solution resistance is measured ~ 18 Ω, the double layer capacitance is determined ~28 µF, and the decay constant of current decay is found to be ~500 µs, which is beyond our temporal resolution.

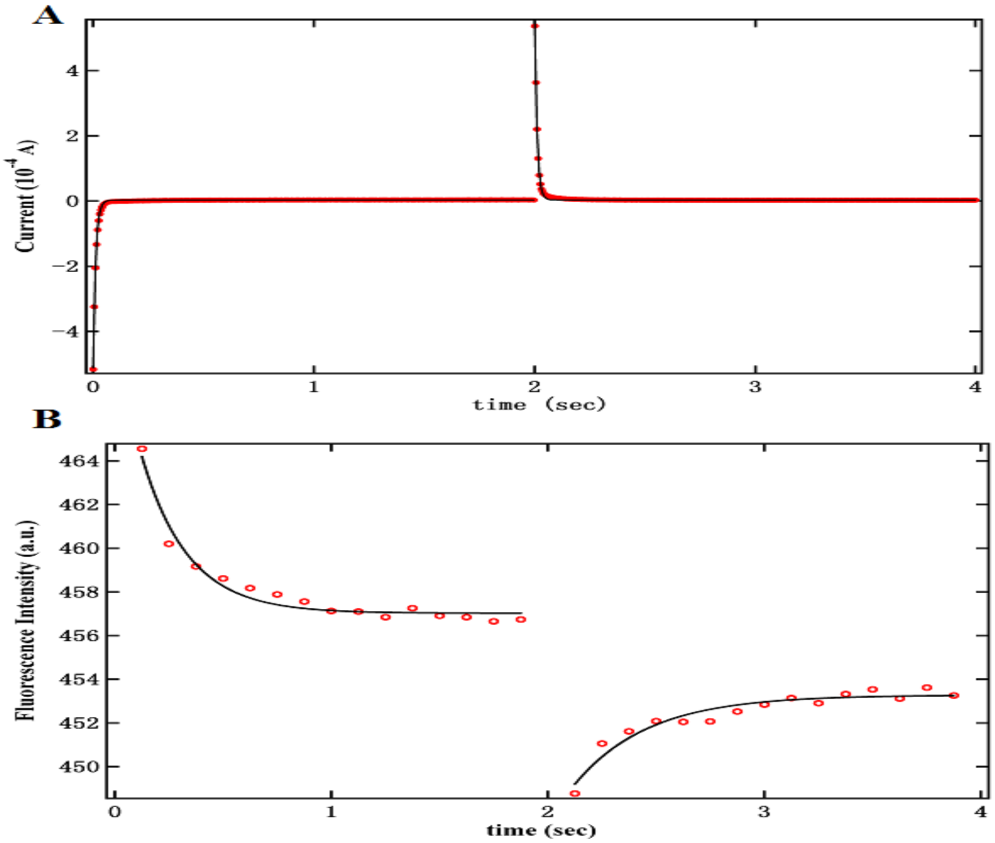

Figure 3-12. A. Red dots are the current response following potential steps. B. Red open circle is the fluorescence signal in response to the potential steps. The black lines in both figures are the exponential fitting curve.

3.1.4 Zwitterion effect

As discussed before, it is the electric field generated by the applied bias that modulates the DNA switching. According to Helmhotz model, at the electrode-solution boundary, the counter ions accumulate within EDL and screen out most of the potential generated by the charged surface. In other words, the electric field mainly acts only strongly within the EDL. For a uniform field, the field strength (E) could be approximately defined as

$$E = \frac{V}{d} \qquad \textbf{(3.18)}$$

d here is the thickness of EDL; V is the applied bias.

Rant et al. have tried to vary *d* from 10 nm to 0.3 nm, but they did not try extreme large *d*. Here we tried experiment with 10 mM 2-(N-morpholino)ethanesulfonic acid (MES) buffer. MES is amino-sulfonic acid based zwitterion buffer which carries equal positive and negative charges at different atoms in each molecule. The advantage of zwitterion buffer is that it does not accumulate near electrode as counter ions to compensate the charges on electrode. Thus the electric field could extend to counter electrode which makes *d* as large as the cell thickness (i.e. 200 μm in our experiments). Alternatively, it could be understood as that the charge number of one MES molecule is zero. Consequently, the ionic strength is zero and the EDL thickness is infinite until the electric field reaches counter electrode. The field strength in MES buffer is only 10V/cm, about 2000 times less than that in the EDL with 0.0067X PBS buffer. As a result, the electrostatic force that acts on the rigid dsDNA rod in zwitterion buffer is negligible as compared to the thermal energy. As entropic effects dominate the DNA behavior, the alignment effect from the electric field is diminished. As expected, it did not show the fluorescence signal modulation when the potential steps were applied (Figure 3-13) in our experiments.

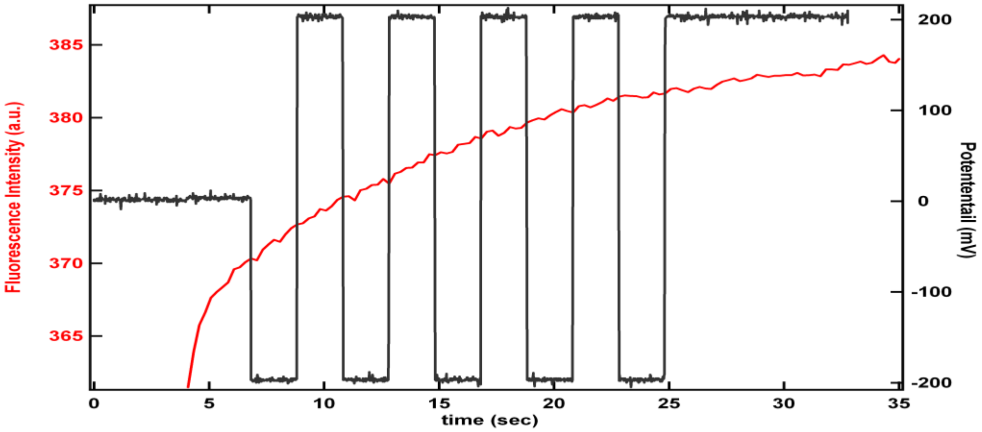

Figure 3-13. Fluorescence response (Red line) to the potential steps (black line) in 10mM MES buffer (zwitterion).

3.1.5 Measurement of DNA density on glassy carbon surface

3.1.2.1 Electrode capacitance

Electrode capacitance could be measured by CV. When applying a potential sweep, a charging/discharging current will be generated as defined by $i = v \bullet c_d$, where ν is the potential scan rate. This charging/discharging current could be used to estimate the electrode capacitance. In this study (Figure3-14), CV have been investigated in 10mM Tris-HCl buffer with four kinds of electrodes prepared by the procedure described in earlier chapter. The potential scan range was +0.25 V to -0.25 V and the scan rate was 100 mV/sec.

The electric double layer capacitance decreases with increasing separation between electrode reactive surface and the diffuse layer. Also, it decreases with decreasing the dielectric constant of the materials in between the electrode surface and the diffuse layer. Comparison of the capacitance of Hexylamine passivated electrode to bare glassy carbon electrode capacitance shows that the Hexylamine layer helped to block the solvent and the ions from accessing the electrode surface. Further, this small decrease of capacitance (21.5%) provided evidence that the passivating monolayer has defects such as pinholes or grain boundaries. A further decrease of capacitance in DNA/Hexylamine modified electrode compared to pure Hexylamine modified electrode indicates a decrease of ionic permeability in the DNA/Hexylamine system. This may be attributed to large DNA molecules that cover part of the defects of the Hexylamine monolayer. The cyclic voltammetry plots of ssDNA and dsDNA modified electrodes almost overlap with each other, indicating that the mixed layer structures are similar.

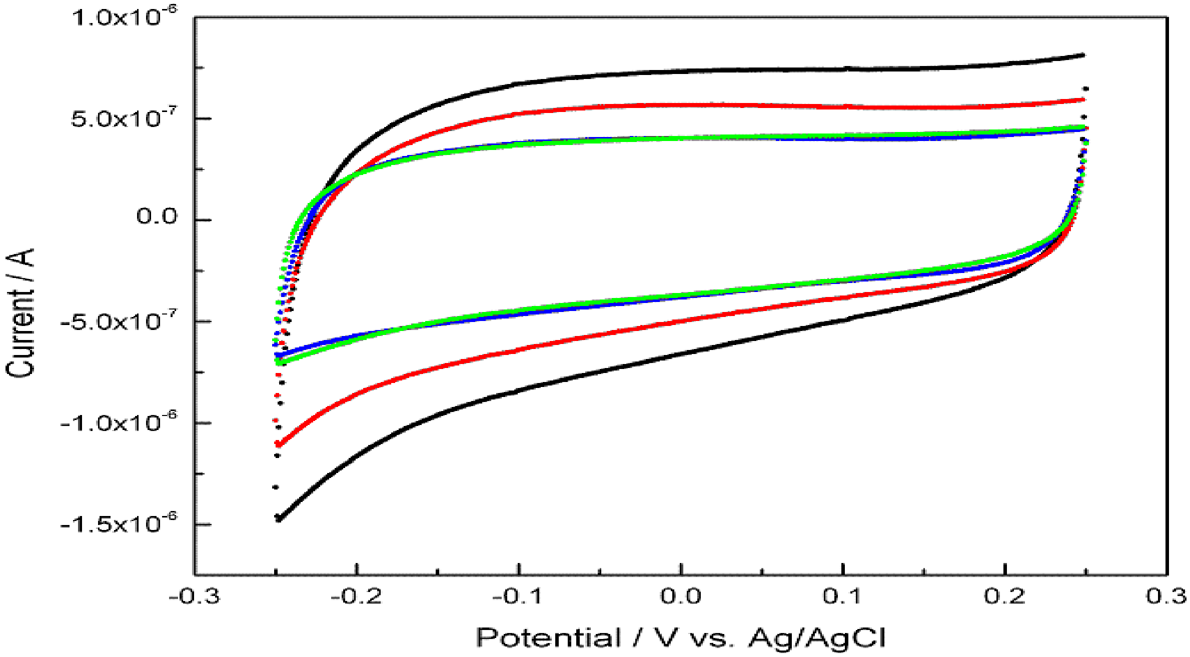

Figure 3-14 Cyclic voltammograms plots of four kinds of electrodes. Black dot, the bare glassy carbon electrode. Red dot, Hexylamine modified electrode. Green dot, P1 + Hexylamine modified electrode. Blue dot, P1+T1+Hexylamine modified electrode.

3.1.2.2 DNA density

Chronocoulometry is the measurement of current integration (Charge Q) vs. time as a step waveform potential is applied. It is the classic electrochemical method to probe the electrode surface properties including the surface absorbed species.[65] Chronocoulometry usually starts at an initial potential where there is no electrolysis. Then the potential instantaneously steps to and holds at a final potential where the oxidization or reduction reaction rate is limited by the mass transfer. For a planar electrode with redox makers adsorbed on the surface, the total charge (Q) measured in chronocoulometry is the sum of charging of the double layer (Q_{dl}), electrolysis of the surface adsorbed redox makers (Q_{ads}) and the electrolysis of the diffusing redox makers in the solution far away from the electrode surface ($Q_{diffuse}$). The charging of double layer and electrolysis of surface adsorbed species finishes instantly as the potential is stepped to the final value and they are time independent. For the solution diffusive species, they must diffuse to the electrode surface to react, and the kinetic is time dependent. The current response for the diffuse redox species could be quantified by Cottrell equation:[66-68]

$$i = nFAC_0 \left(\frac{D}{\pi t}\right)^{1/2} \tag{3.19}$$

The integration from t=0 gives the charge response which is linearly proportional to $t^{1/2}$:

$$Q = 2nFAC_0 \left(\frac{D}{\pi}\right)^{1/2} t^{1/2} \tag{3.20}$$

The charge of the surface adsorbed redox species could be quantified as:

$$Q_{ads} = nFA\Gamma_0 \tag{3.21}$$

$$Q_{total} = Q_{ads} + Q_{dl} + Q_{diffuse} \tag{3.22}$$

The typical chronocoulometry plot is Q_{total} vs. $t^{1/2}$. The intercept at $t^{1/2} = 0$ is the sum of Q_{dl} and Q_{ads}.

Steel et al. has published a method to quantify surface DNA density immobilized on gold electrode based on chronocoulometry.[67] This method could precisely determine the density which is between $1\text{x}10^{12}$ and $10\text{x}10^{12}$ DNA/cm^2. When DNA modified electrode is exposed to 50 µM hexaammineruthenium (III) chloride ($Ru(NH_3)_6^{3+}$) 10 mM Tris-HCl buffer, the surface confined DNA strongly traps $Ru(NH_3)_6^{3+}$ through electrostatic interaction. Under this condition, every $Ru(NH_3)_6^{3+}$ compensates the negative charge of every three phosphates, and the all the negative charge on DNA is neutralized. Hence, in chronocoulometry, the quantity of the charge of DNA trapped Ru $^{3+}$ (Q_{ads}) could be converted into the quantity of DNA density through the relationship:[67, 68]

$$\Gamma_{DNA} = \Gamma_0 \left(\frac{Z}{m} \right) N_A = \frac{Q_{ads}}{nFA} \times (\frac{Z}{m}) \times N_A \qquad \textbf{(3.23)}$$

Here n is the number of electrons involved in redox reaction per molecule ($n = 1$ for $Ru(NH_3)_6^{3+}$ reduction), Z=3 represents every three nucleotides compensated by one $Ru(NH_3)_6^{3+}$, and m is the total number of nucleotides ($m = 34$ for 34-mer ssDNA and $m = 68$ for 34-mer dsDNA)..

n this study, both ssDNA (Figure3-15-A) and dsDNA (Figure 3-15-B) modified electrodes have been investigated in the same electrochemical cell. The Q_{ads} for ssDNA is 0.4085 C and for dsDNA is 0.5239 C. This translates into an average spacing between neighboring ssDNAs of 6.3 nm and a density of 3.2x10^{12} ssDNA/cm^2. For dsDNA, the average spacing is 7.9 nm and the density is 2.0x10^{12} dsDNA/cm^2. The ssDNA modified electrode has higher DNA density than dsDNA modified electrode. This is because the hybridization efficiency from ssDNA to dsDNA is not 100%. About 63% of the ssDNA has been hybridized with the target. In Rant's study, they always kept the DNA density at around 10^{11} DNA/cm^2 and their observed fluorescence is over a larger area with an average over 3x10^8 DNA. In our case, the glassy carbon electrode surface is quite inhomogeneous so that the local DNA density will be higher than the calculated value, and our observed fluorescence is only over 1x10^5 DNA.

For our P1+T1/Hexylamine modified glassy carbon electrode, the microscopic structure of the electrode surface could be described as a mixed layer of ssDNA, dsDNA, Hexylamine and defects as pinholes, boundary grains. The distance between the DNAs is around 6.3 nm, which indicates that there is significant steric hindrance coming from neighboring DNAs when they are forced to reorient under the electric field.

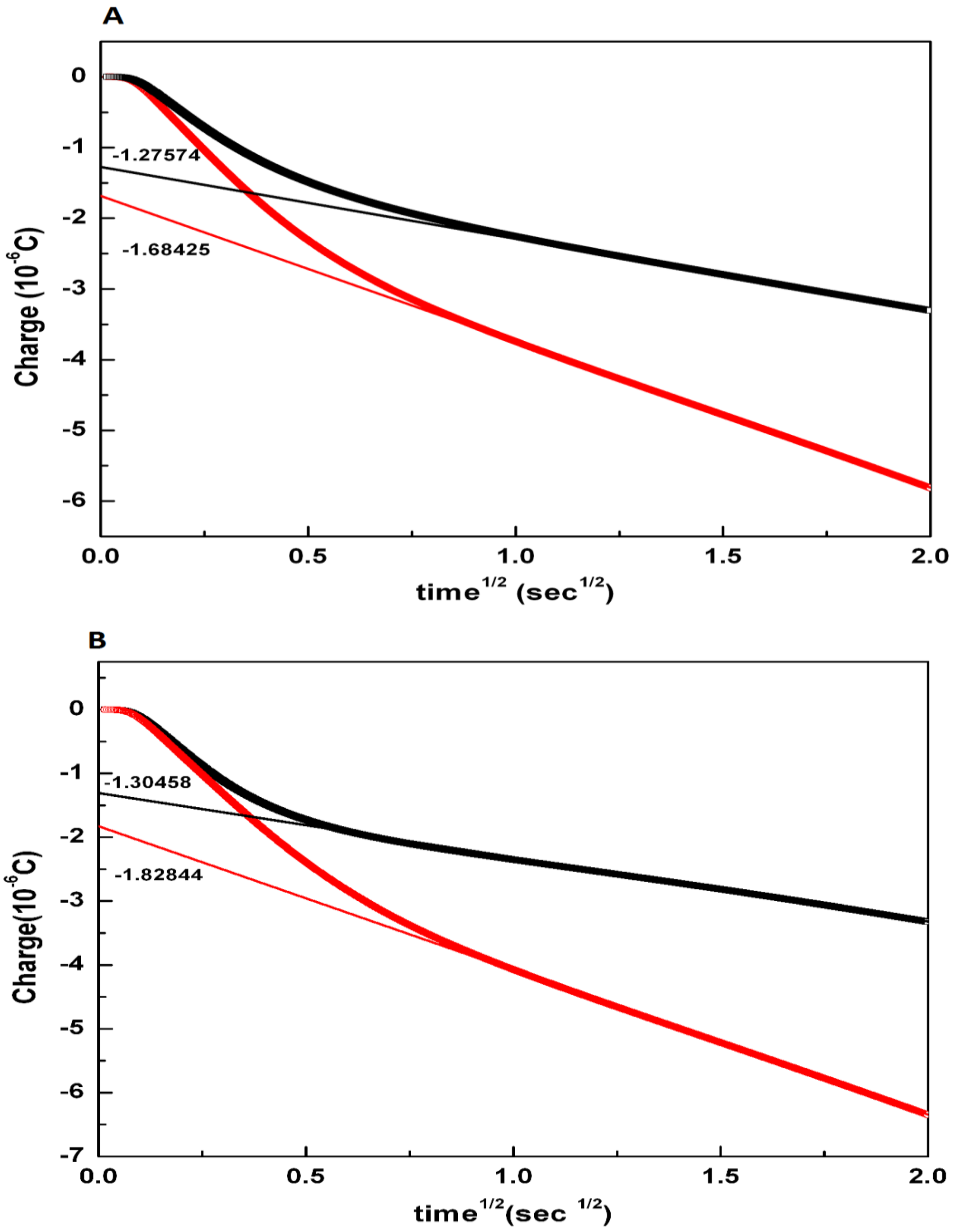

Figure 3-15 Chronocloumetry plots for determining the density of A: ssDNA and B: dsDNA. Black dots are measurements without Ru(III) and red dots with Ru(III). The black and red lines are linear fitting curves for the data points after 1 second.

3.1.5 Hypothesis of DNA reorientation model and preliminary explanations

Summarizing the experimental results that we have gotten so far, we can draw the following conclusions:

1. Strong electric field could drive DNA switching and the driven effect depends on the ionic strength.
2. Electric field could not drive DNA switching when the electrolyte contained only zwitterion buffers.
3. The reorientation of DNA is slower than the charging/discharging process of EDL.
4. The structure of glassy carbon surface is rather complicated. First, most area of glassy carbon is consisted of chemically inert, fullerene-like graphite layer with only a small portion of the surface presents graphite edge plane like structure which is chemically active and covalently modified with DNA. Second, even within the local active area, it is a mixture of ssDNA, dsDNA, imperfect passivation layer. Third, the dsDNA density was too high to avoid the steric effects from neighboring DNA molecules.

Nevertheless, the electric field driven process can be described as followings to explain our experimental results:

Negatively charged DNAs are anchored on glassy carbon surface with a tilt angle (θ) that allows the whole system to reach a statistical energy minimum at the initial OCP (Figure 3-16-A). As -0.2 V vs. OCP is applied, the electrode generates negative charges at the electrode side. The induced charge disturbs the ion distribution at the electrode-solution boundary causing more positively charged ions accumulate at the solution side while negatively charged ions are repelled and move away from the boundary, thus forms a gradient positive ion distribution profile, i.e. the electric double layer (EDL). As the EDL screens most of the induced charge within a short distance (nm range), it produces an extremely strong electric field. This electric field overcomes thermal energy (k_BT) thus repels DNAs away from the electrode surface to reduce the total energy of the system. As a result, the end tethered DNAs “stand up”. At this point, the DNAs at the electrode surface change from a highly disordered system to a more ordered one (Figure 3-16-B). Immediately after potential stepping, DNA plays as a part of the anions to constitute the EDL. As DNA moves away from the electrode surface, the "real" thinner EDL is established. During this process, more cations moves toward the electrode and compensates the negative induced charge at the electrode side as well as the negative charge on DNAs, thus reduces the electrostatic interaction between DNAs and electric field (Figure 3-16-C). If treating DNA as a close system, the entropy prefers to increase by disturbing the order. Also the Brownian motion of ions, solvent molecules, and DNAs disturbs the “stand up” status. As a consequence, DNAs start to tilt. The tilting process is impeded by neighboring DNAs. Not only has the steric effect increased as DNA tilting, but also the electrostatic repulsion between the negatively charged DNA backbones (Figure 3-16-D).

As +0.2 V vs. OCP is applied, the induced charge at the electrode side also rearranges the anions distribution profile. As a result, negatively charged DNAs are attracted to “lie down” on the electrode surface, serving as a part of the anions in EDL to compensate the positive induced charge (Figure 3-17-B) at the electrode side. If no other anions available, DNAs would stay at “lay down” position even though they prefer the tilt energy minimum position. But in fact, the anions in bulk solution will diffuse into EDL to take place of DNAs. As more and more anions diffuse into EDL from the bulk solution, DNAs are released from electrode surface, tilting back toward the energy minimum position. As DNA moves away in the relaxation step, the EDL is getting thicker (Figure3-17-C).

We can also apply the above model to explain the effects of ionic strength on dsDNA reorientation. Taking 0.0067X and 0.2X PBS buffer for example, the expected thickness of the EDL is 10 nm and 1.8 nm, respectively. As -0.2 V vs. OCP is applied, 34-mer dsDNA in length of 11.92 nm was forced to stand up. For 0.0067X PBS buffer, 90% of the negatively charged dsDNA backbone locates within EDL and is surrounded by the excess cations, while for 0.2X PBS buffer, only 16% of dsDNA is within the EDL, causing very different electrostatic repelling effects. When dsDNA starts to tilt back, they should experience similar steric effects in these two buffers since the DNA density is the same. However, the negative charges in dsDNA backbone outside the EDL now tends to bring excess anions back into the already equilibrated EDL and thus encounters a second repelling electrostatic force from EDL as well as neighboring DNAs. For 0.0067X PBS buffer, only 10% of the negative charge on the backbone acts, while for 0.2X PBS buffer, 84% of the negative charge on the backbone repel DNA tilt. Clearly, in lower ionic strength buffers with thicker EDL, DNA experienced less electrostatic repulsion thus tilt back faster than those in higher ionic strength buffer. When applying attraction potential step, no matter in which buffer, the dsDNA molecules lie down within EDL. How fast it could be released from the electrode surface is determined by the rate at which the anions in bulk solution diffuse into EDL to take place of charges on DNAs. With the same diffusion constant, buffer of higher concentration could supply more anions in unit time than buffer of lower concentration. Thus, DNA in lower ionic strength buffer tilts slower than those in higher ionic strength buffer.

Above discussions are based on following assumptions: (1) DNAs presents an average tile angle from the electrode surface at the energy minimum position; (2) DNA could be treated as a close system after the equilibrium of EDL has been established. But whether these are true needs to be validated with more studies with physical and computational chemistry. For future work of this project, besides the computational study, more experimental work could be explored.

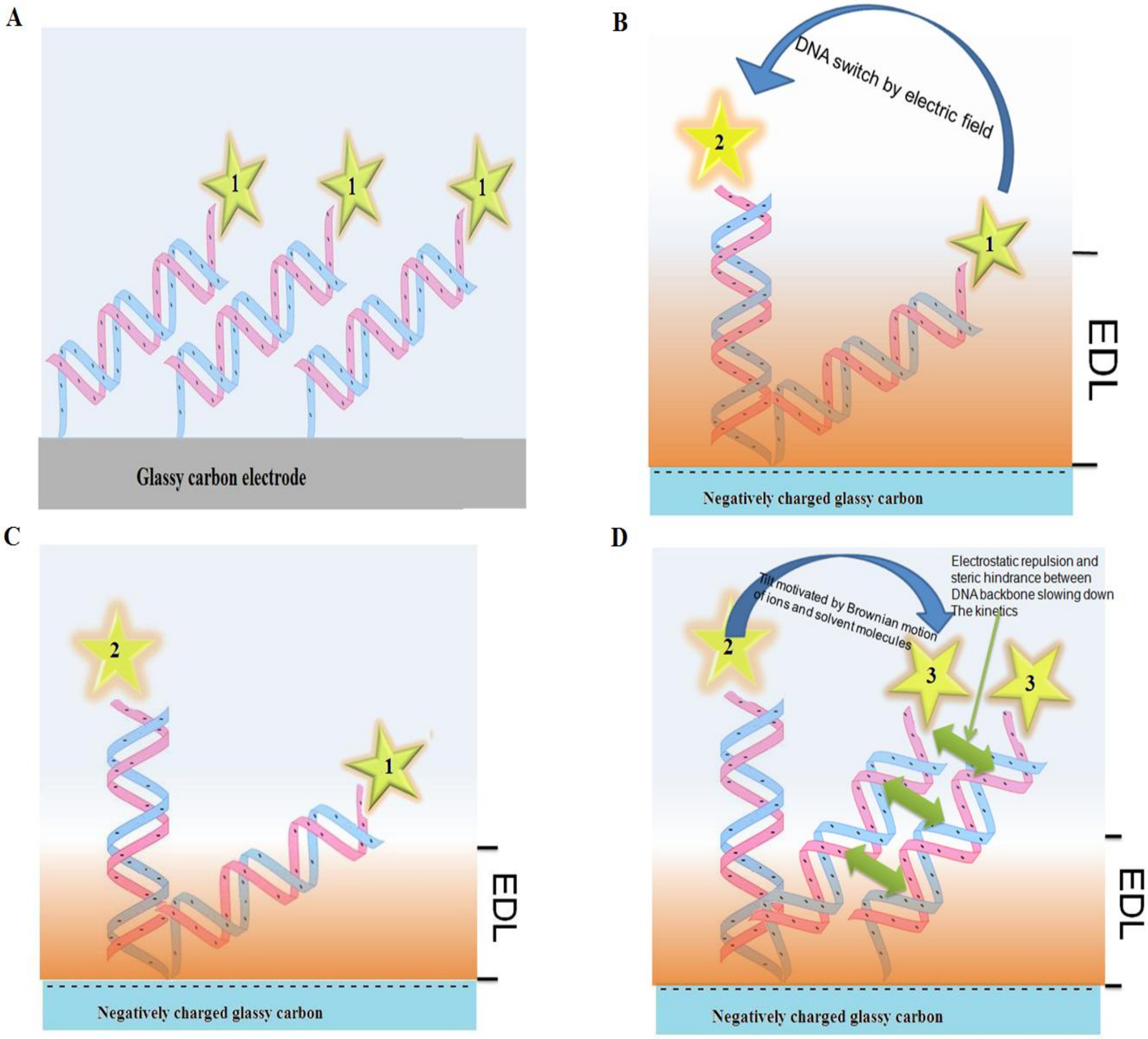

Figure 3-16 Schematic of the dynamic processes of dsDNA switching and reorientation at negative potentials. A. At OCP, dsDNAs stay at the engery minimum position (i.e. position 1). B. As a negative bias is applied, the dsDNA quickly switches from position 1 to position 2. C. The EDL becomes thinner as DNA moves away from the electrode surface. D. After the EDL establishes the equilibrium, the slower Brownian motion starts to show effects. Each dsDNA also receives the steric effects and electrostatic repulsion from the EDL and neighboring dsDNAs.

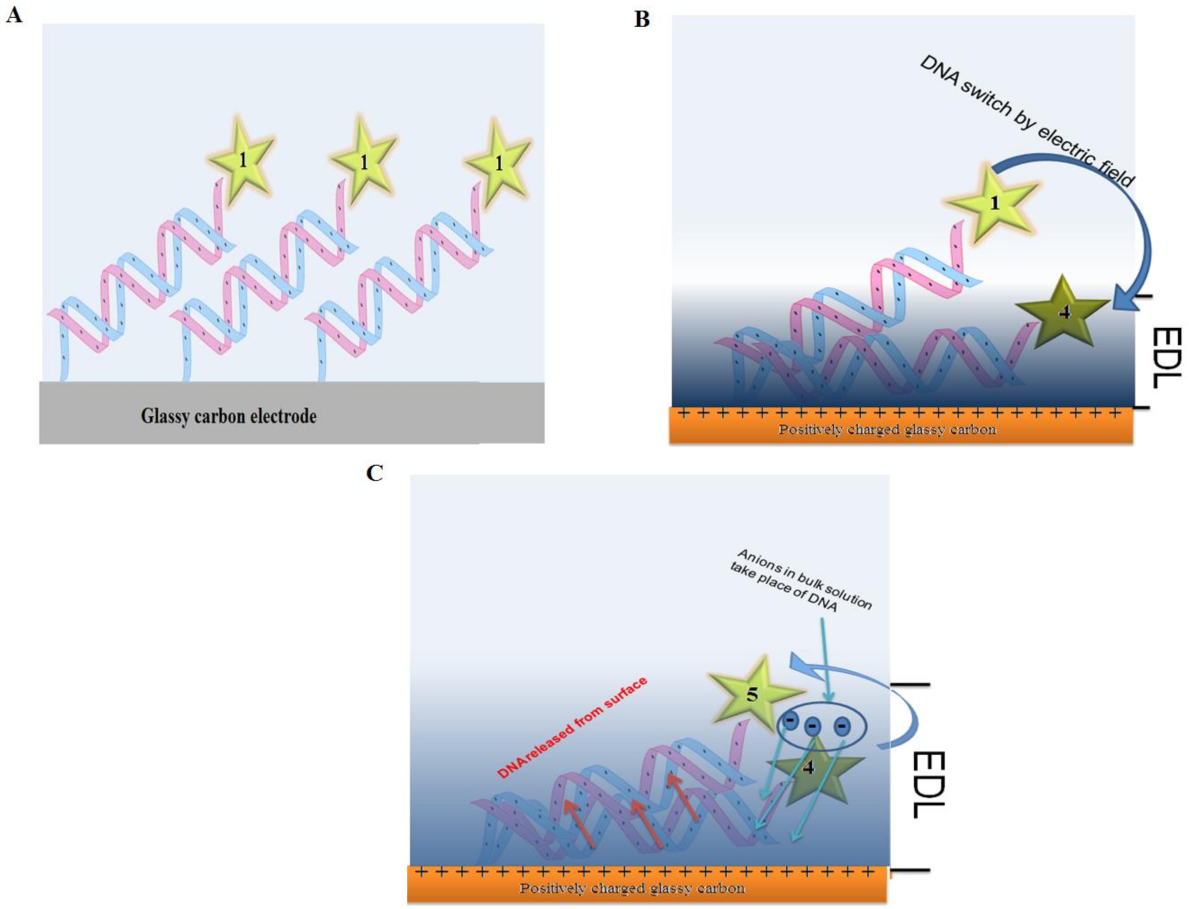

Figure 3-17 Schematic of the dynamic processes of the dsDNA switching and reorientation at positive potentials. A. dsDNAs stay at the energy minimum position (i.e. position 1). B. dsDNA quickly switches from position 1 to 4 as a positive potential is applied. C. dsDNA reorients from position 4 to 5 as the bulk anions diffuse into EDL to take place of the negative charge in dsDNA.

3.2 EIS detection of DNA hybridization

3.2.1 Normal EIS detection of DNA hybridization based on patterned CNF array

3.2.1.1 Electrochemical cell and patterned CNF array

EIS study is carried out with a multiplex CNF nanoelectrode array chip in an individually addressed “array-in-array” format. The chip is provided by Early Warning Inc. and the electrochemical cell (Figure 3-18-A) is provided by Dr. Bruce Gale's group at the University of Utah through a grant provided by Early Warning Inc.

The patterned CNF array chip has 3x3 individually addressed electrode pads (200 µm X 200 µm) (Figure 3-18-B,C). SEM images show that CNFs stick out of SiO_2 surface by ~500 nm (Figure3-18-D). CNFs are patterned into a regular array with a spacing of 1 µm at each pad. The 3x3 electrode pads were connected with external contact pads (1 mm X 1mm) through the metallic line underneath the SiO_2 layer.[69-71]

Electrochemical cell has two parts (Figure 3-18-A). Bottom part has a reservoir to locate the chip at fixed position. Top part has a print circuit board (PCB) connecting 9 small spring-loaded copper spins with the 9 contact pads. The cell seals against the CNF array chip through an O-ring with 1 cm in diameter.

3.2.1.2 Precondition of patterned CNF array and characterization by SEM and CV

The received patterned CNFs are covered with polymer layers after the treatment of RIE. Efforts are required to remove the polymer layer and activate CNF electrodes. Usually, CNFs after RIE treatment will be first immersed in 1M HNO_3, followed by thermal annealing at 375 ^{o}C and electrochemical etching in 1 M NaOH. Among these treatments, electrochemical etching in 1M NaOH is the most important step.

Cyclic voltammetry with 4 mM $K_4Fe(CN)_6$ and 1 M KCl has been used for characterization of electrodes. The current peak density of redox molecules in CV of a hemispherical diffusion model of a disk-like electrode could be defined as the sum of planar diffusion and radial diffusion as following:

$$\frac{i_{peak}}{A} = 0.446 nFC_0 * \sqrt{\frac{nFD_0\upsilon}{RT}} + nFC_0 * (\frac{D_0}{r}) \qquad \textbf{(3.24)}$$

Here n is number of electrons involved in each redox molecule; F is the Faraday constant; R is the molar gas constant; T is the temperature; D_0 is the diffusion constant; C_0 is the bulk concentration of redox molecules; A is the active electrode area; r is the radius of the electrode; and υ is the scan rate of cyclic voltammetry.

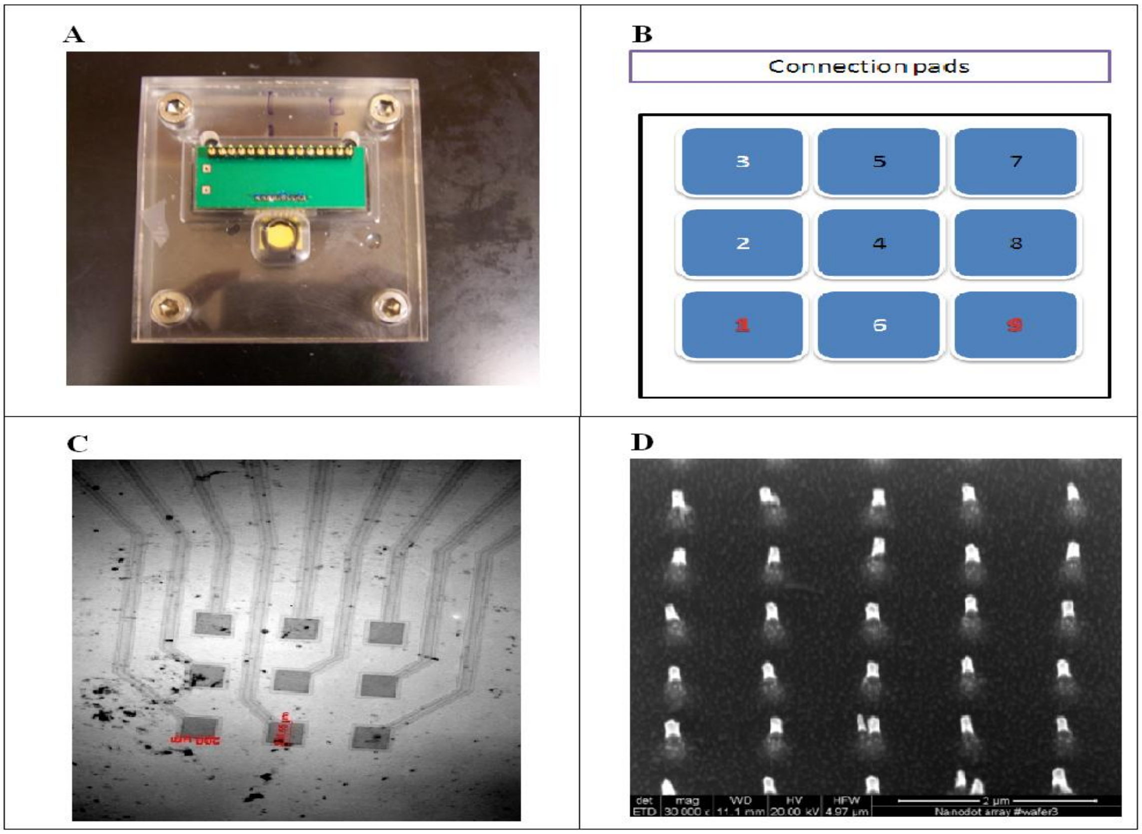

Figure 3-18. . A photograph of the electrochemistry cell fabricated by the University of Utah specifically used for testing patterned CNF arrays. B. A schematic drawing of the 3x3 electrode pads and the index of each pad. C. An optical microscopic image taken with a 4X objective to show the 3x3 electrode pads and the metal lines for electrical connection. Each pad is around 200 µm X 200 µm. D. A SEM image of one electrode pad. The brighter materials are the exposed CNFs. All CNFs are well encapsulated by SiO_2 except the exposed tips. The scale bar is 2 µm.

The first part of the equation describes the linear diffusion, it is proportional to the square root of scan rate, and in CV plot this could be characterized by a well defined diffusion controlled peak. The second part describes the nonlinear radial diffusion; it increases as the electrode radius is reduced. In CV plot, it could be represented by a sigmoidal shape giving a steady-state current. As the electrode size is reduced to nanoscale, the second term dominates. A sigmoid shape I-V curve with small separation in forward and reverse scans is what is expected for the patterned CNF array.

To verify the electrochemical etching condition, we divided the 9 electrode pads into 4 groups (Figure3-19-A). After immersing in 1.0 M HNO_3 for 15 minutes, pad 3, 5, 7 received no further treatment; pad 4 and 8 were etched in 1.0 M NaOH at 1.2 V for 20 seconds; pad 2 and 6 were etched in 1.0 M NaOH at 1.3 V for 20 seconds; pad 1and 9 were etched in 1.0 M NaOH by CV between -0.1 V and 1.3 V with a scan rate of 0.05 V/s for 6 times. Figure 3-19-B is the combination of SEM images from the 9 electrode pads. Clearly, pad 3, 5, 7 show no electrochemical etching with the CNFs still sticking out. Pad 4 and 8 are consistent with each other, both of them have been partially etched with CNF etched at the junction with SiO_2 surface. The partially etched CNFs lie down on SiO_2 surface forming "debris" features. Pad 2 and 6 are also consistent, but pad 2 looks like being etched more than pad 6. Pad 1 and 9 etched by CV method are not consistent. Pad 1 has only been partially etched; but pad 9 has been totally etched away, eaving "recessed" CNFs.

The high-resolution SEM image of the "debris" feature (Figure3-19-C) indicates that it may be due to the "polymer" formed in RIE step. We found that such "debres" could be easily removed by gently wiping the chip with a wet Q-tip. Figure 3-19-D is the SEM image of pad 8 after wiping with a Q-tip. All CNFs are leveled at the SiO_2 surface.

Combining SEM and CV results, we are confident that the following steps can reliably produce active CNFs in the patterned array. Step1, soak in 1 M HNO_3 for 10 – 15 minutes; step 2, etch in 1 M NaOH at 1.2 V for 20 seconds; step 3, gently wipe with a wet Q-tip.

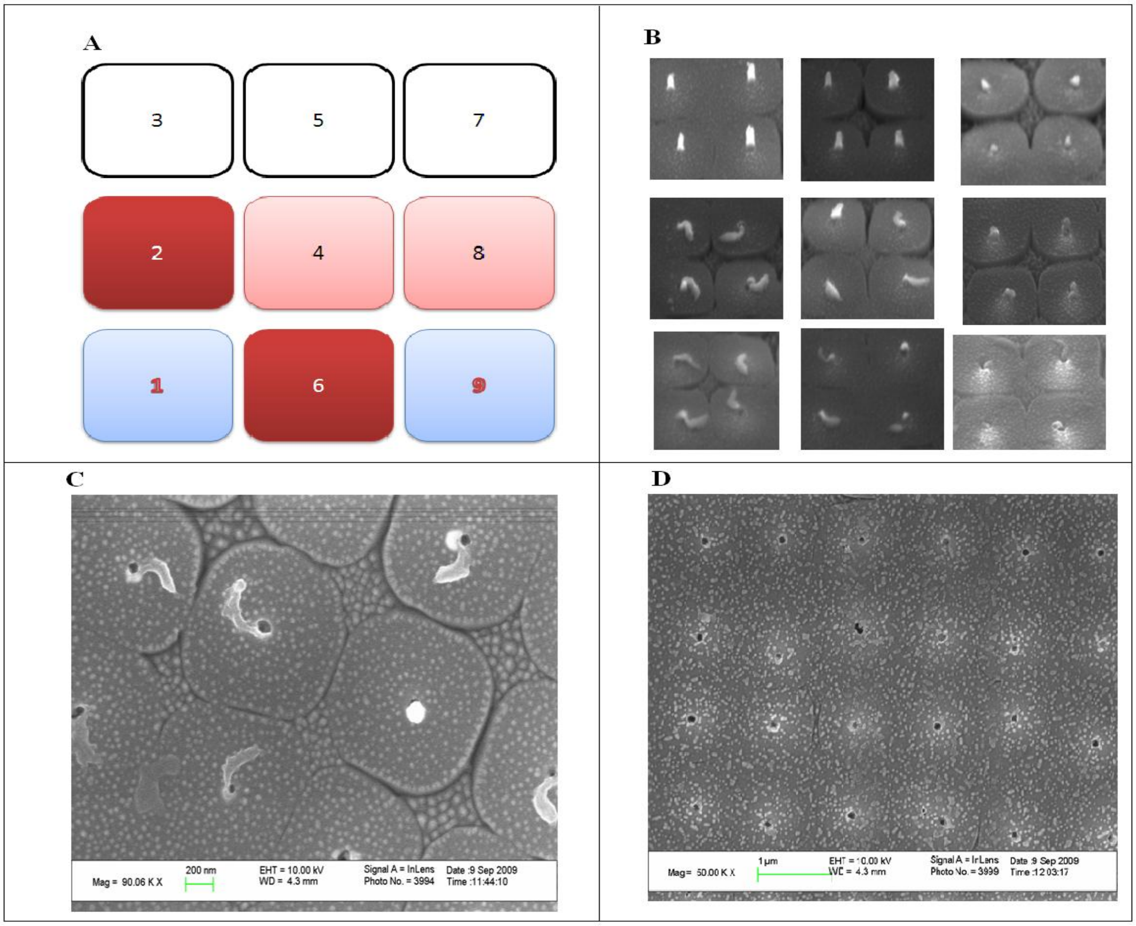

Figure 3-19. Pretreatment of CNF arrays with 1 M NaOH. A. The index of the electrode pads. Pads with the same color received the same treatment. B. SEM images corresponding to each pad in A. C. A high-magnification SEM image of pad 8 to show the detailed "debris" features. D. A SEM image of pad 8 after wiping with a Q-tip.

3.2.1.3 Detection of DNA hybridization by EIS

Figure 3-20-A&B are the CV plots of all 9 pads before and after the preconditioning treatment that we just discussed. It shows that the electrodes have been activated as desired. The CNF arrays could be then used for DNA functionalization and hybridization detection.

Step1: Modifying CNF with DNA probe P3. The activated electrodes were modified with 5 μM P3 catalyzed by NHS and EDC in 1 X PBS buffer at 40 ^{o}C for 24 hours. EIS (Figure 3-21-A, solid black square) was measured in 1 mM $K_4Fe(CN)_6$ and 1 mM $K_3Fe(CN)_6$ in 1X PBS buffer.

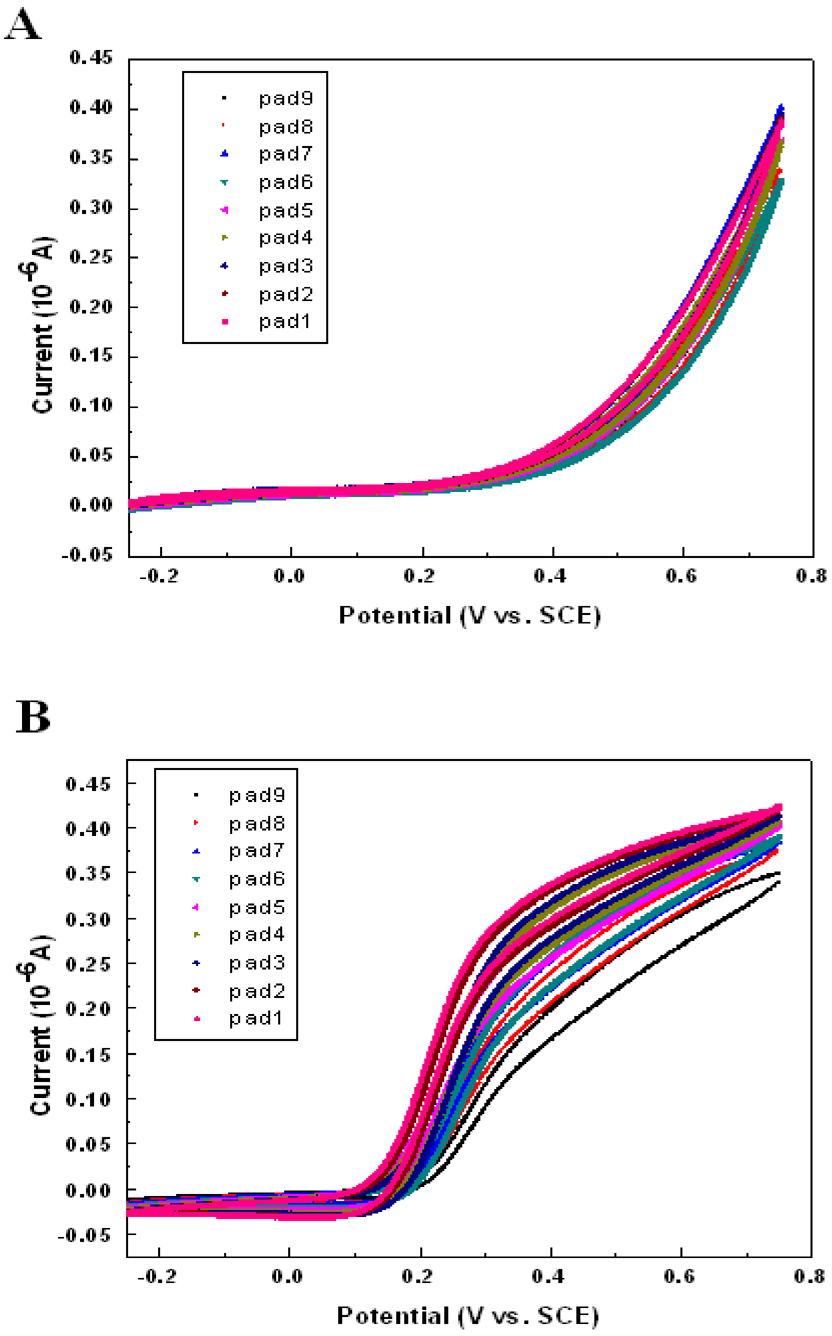

Figure 3-20 Cyclic voltamograms of patterned CNF arrays before any treatment (A) and after a series of treatments as shown in Figure 3-19 (B). CV was performed in 4 mM $K_4Fe(CN)_6$ in 1 M KCl. The scan rate was 0.05 V/s.

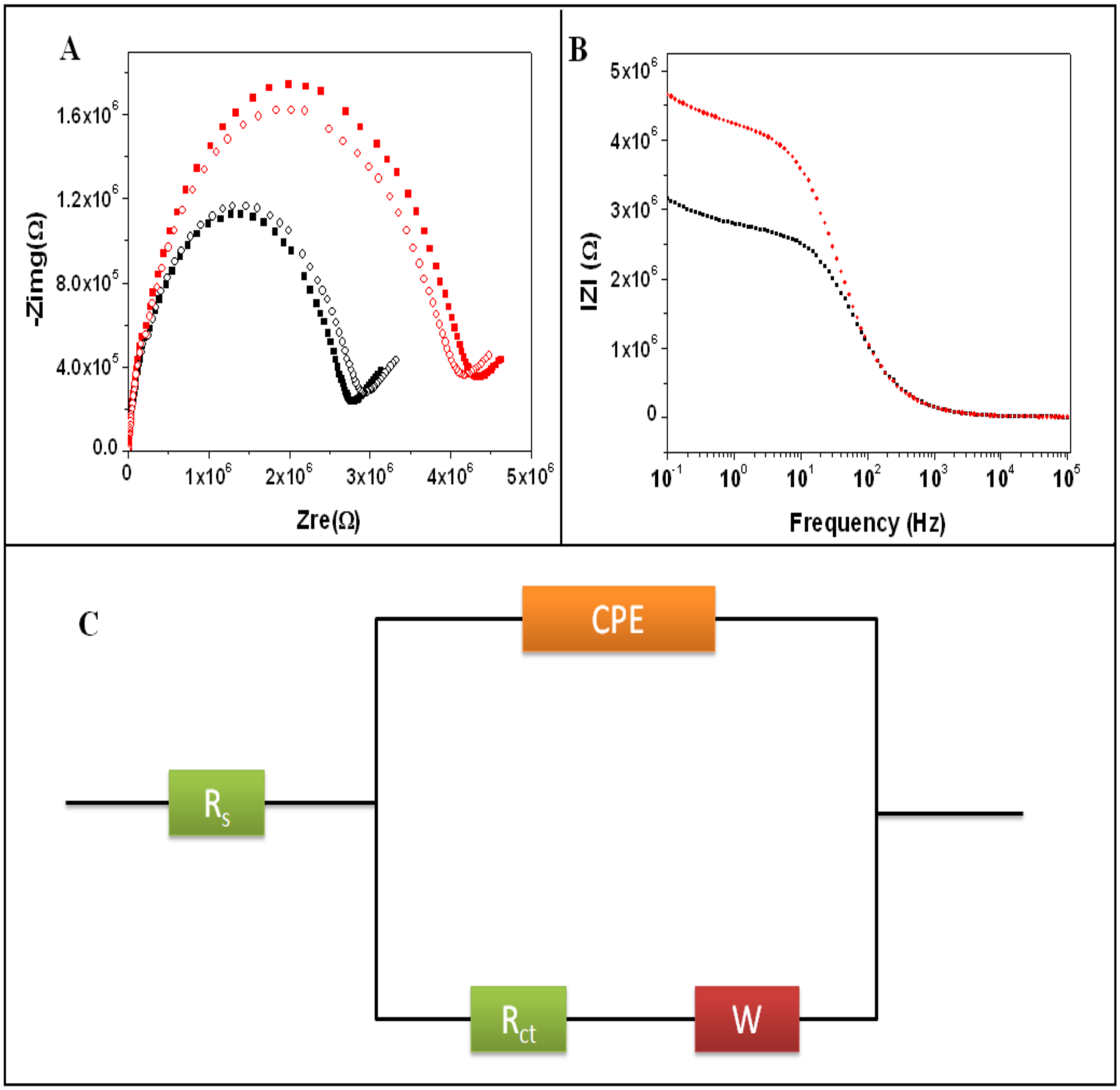

Figure 3-21 EIS detection of DNA hybridization on patterned CNF arrays. A. Nyquist plot of EIS. Black solid square is the EIS of CNF+ P3; red solid circle is the EIS of CNF+P3+T3; black open square is the EIS of CNF+P3 which is the product after denaturing P3+T3 dsDNA; red open circle is the EIS of CNF+P3+T3 after the rehybridization. B. the Bode plot, red solid square is the dsDNA and black solid square is the ssDNA; C. An equivalent circuit that could be used to describe the physical model of the cell. All EIS spectra were taken in 1 mM $Fe(CN)_6^{4-}$ and 1 mM $Fe(CN)_6^{3-}$ in 1X PBS buffer. The AC amplitude of EIS was 10 mV rms, DC bias was 0 V vs. OCP, frequency range was 100 kHz to 100 mHz.

The parameters for EIS were: AC amplitude 10 mV rms; DC bias 0 V vs OCP; frequency range 100 kHz to 100 mHz, which resulted in the whole measurement in less than 2 minutes.

Step 2: Hybridizing P3 with T3. Chip was immersed in 2.5 μM T3 in 3X SSC buffer at 40 ^{o}C for 2 hours. EIS spectrum (Figure3-21-A, solid red circle) was recorded under the same condition as mentioned in step 1.

Step 3: Dehybridizing T3 from chip. To verify whether the chip is reusable, we denatured the P3+T3 dsDNA in 1 X PBS buffer at 90 ^{o}C for 10 minutes, and cooled down to room temperature. EIS (Figure3-21-A, open black square) was measured with the same conditions as above.

Step 4: Rehybridizing T3 with P3 under the same conditions of step2. EIS was measured (Figure 3-21-A, red open circle).

All EIS spectra could be nicely fit with an equivalent circuit as shown in Figure 3-21-C. R_s represents the solution resistance; CPE is a capacitor-like element; R_{ct} is the charge transfer resistance; W is the Warburg impedance.

The fitting results indicate that R_{ct} is the most sensitive component in the circuit in response to DNA hybridization. R_{ct} for CNF only modified with P3 is 2730 kΩ, while after hybridizing with T3, R_{ct} dramatically increases to 4245 kΩ. Two reasons could account for the increase of R_{ct}. First, dsDNA blocks the electrode surface more than ssDNA due to the large size. Second, dsDNA repels negative charged mediator more efficiently than ssDNA because there are more negative charges on dsDNA backbone than ssDNA.

R_{ct} for the denatured sample dropped to 2831 kΩ, and after rehybrization, it increased back to 4005 kΩ. Clearly, the chip is reusable if properly denaturized. And it is clear from the Bode plot (Figure 3-21-B) that this method could distinguish ss- and ds-DNA at low frequency region (< 50 Hz).

3.2.2 Impedance methods detection of DNA hybridization under high AC amplitude

Normally, the AC amplitude of EIS is controlled below 50 mV in order to avoid large disturb to the electrode—solution interface. Recently, Siddiqui has demonstrated EIS may also work even under high AC amplitude when scaling down the electrode size. [69]. Their results showed that the charge transfer resistance kept almost the same as AC amplitude increased from 10 mV to 100 mV on patterned CNF array. [69] Also, Rant's research showed that ssDNA and dsDNA could be distinguished even at high frequency region by monitoring the fluorescence signal driven by electric field due to their difference in mechanical rigidity. Our research showed that the initial switching of dsDNA under electric field (± 0.2 V vs. OCP) is quite fast since the negatively charged dsDNA is directly involved in the reconstruction of EDL. Our previous study also find that for $V_0 \leq 50mV$, without a redox mediator, the ssDNA and dsDNA could only be distinguished in low frequency range ($\leq 40Hz$), but it is very sensitive to nonspecific adsorption and biofouling. All these inspired us to explore the possibility to detect the DNA hybridization event in real time by utilizing high AC amplitude to drive dsDNA switching at high frequency region.

3.2.2.1 High AC amplitude EIS detection of DNA hybridization on glassy carbon

To achieve the goal above, first we have to demonstrate that high AC amplitude EIS responses to ssDNA and dsDNA differently. We performed EIS measurements in low ionic solution without redox mediators (0.067 X PBS) at high AC amplitude (141 mV rms). The scan range was between 100 kHz and 0.1 Hz, and the DC bias was 0 V vs OCP. Glassy carbon electrode modified with P3 was first measured; and then the same electrode was hybridized with T3, followed by an EIS measurement.

As we expected, even though the Nyquist plots (Z_{img} vs. Z_{re}) of dsDNA and ssDNA almost overlap with each other (Figure3-22-A), the bode plot ($|Z|$vs. frequency) clearly shows $|Z|$ of dsDNA is larger than that of ssDNA for frequency higher than 40 Hz (Figure3-22-B).

High AC amplitude EIS measurements at fixed frequency (100 Hz, 600 Hz, 1000 Hz, 2000 Hz, and 5000Hz) are taken to find the frequency that is most sensitive to DNA hybridization. Difference of $|Z|$ between dsDNA and ssDNA at those 5 frequency points are 2Ω, 6.5Ω, 29Ω, 8Ω, and 37Ω. As a result, 5000 Hz is chosen as the most sensitive frequency for later experiment (Figure3-22-C).

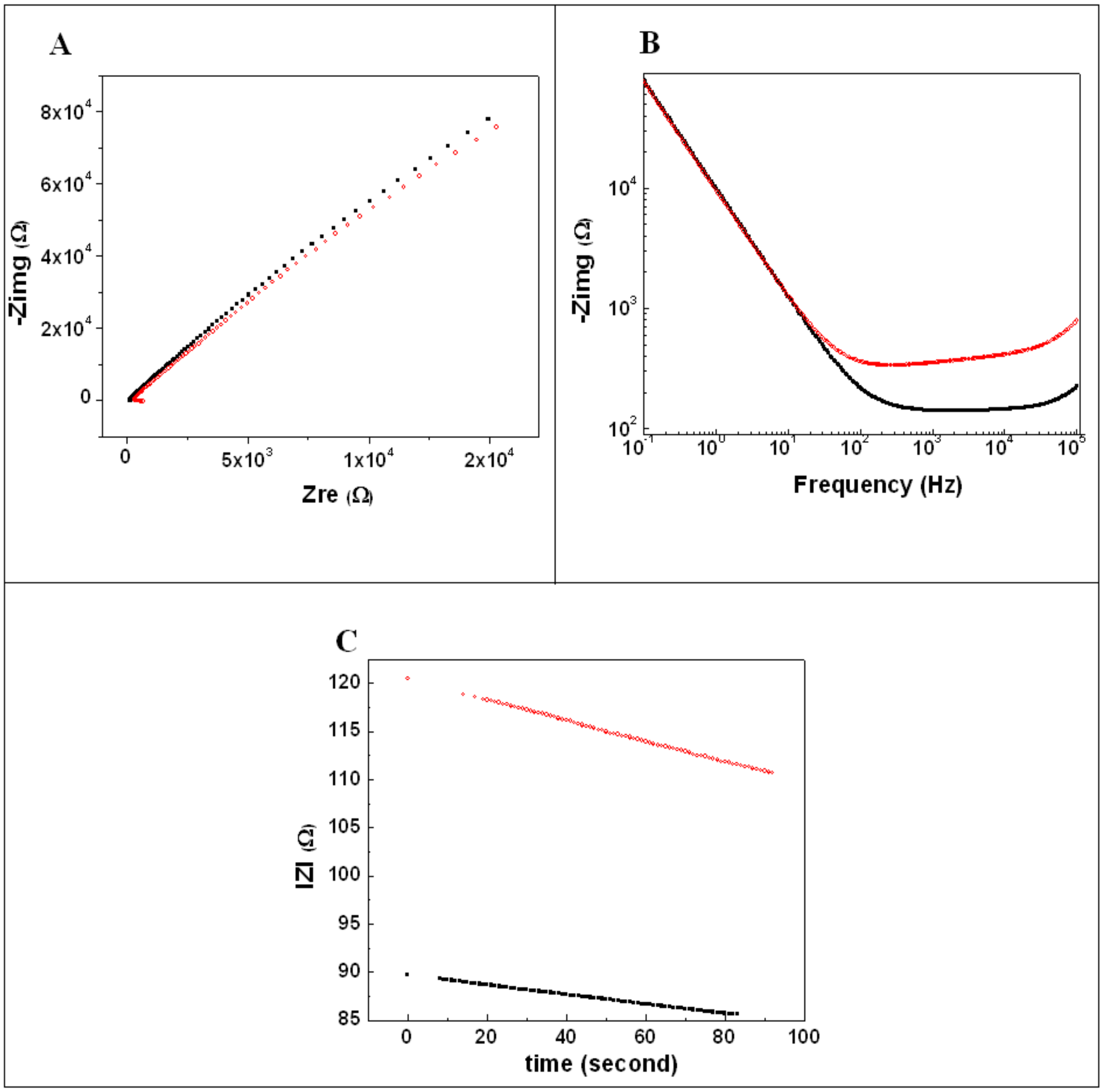

Figure 3-22 . EIS at high AC amplitudes to detect DNA hybridization. A. Nyquist plot and B. Bode plot of EIS spectra. For A and B, the AC amplitude of 141 mV rms, DC bias at 0 V vs. OCP, frequency range of 100 kHz to 0.1 Hz are applied. C. the real-time EIS spectra with fixed frequency at 5000 Hz. Black solid circle is from ssDNA, red solid circle is from dsDNA. All spectra were taken in 0.067 X PBS buffer.

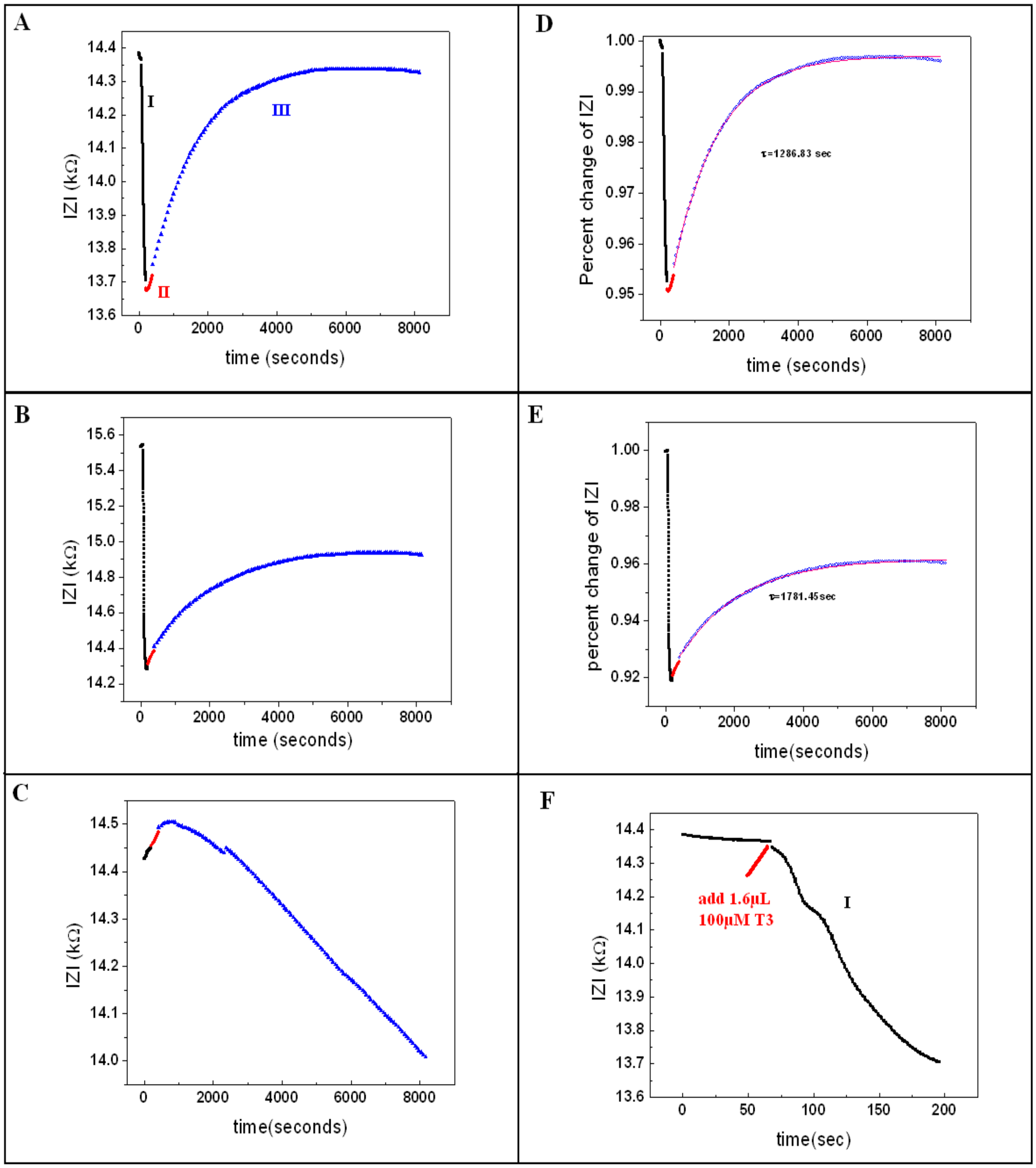

Figure 3-23. Real-time detection of DNA hybridization: A. on P3 modified glassy carbon electrode; B. on bare glassy carbon; and C. adding 0.067 X PBS buffer instead of T3 solution. F is the details of period I of plot A, in which T3 solution was added into the cell at around 50 seconds. D and E, the $|Z|$ normalized with the initial impedance $|Z_0|$, the pink line is the fitting curve of period III.

3.2.2.2 Real-time detection of DNA hybridization

In previous sections, we found that EIS at 141 mV rms, 5000 Hz could well distinguish glassy carbon electrodes modified with dsDNA from those with ssDNA. Now we design a platform that could be used to monitor the hybridization process in situ by real-time EIS (REIS) (Figure 3-23).

Glassy carbon modified with P3 was mounted in a small Teflon cell. There was 160 μL 0.067 X PBS buffer serving as the supporting electrolyte. High AC amplitude REIS at fixed frequency (5000 Hz) was used to record the DNA hybridization. The whole spectrum was divided into 3 periods (Figure 3-23-A). Period I, REIS was taken at 5000 Hz. We observed an instant drop in total impedance when we added 1.6 μL of 100 μM T3 (in 0.067X PBS) solution into the 160 μL electrolyte (Figure 3-23-F). This impedance dropping process lasts for almost 3 minutes. Period II, the impedance stopped droping and started to increase while the REIS experimental condition remains the same. Period III, 128 data points were taken during this period at 5000 Hz with 1 minute interval between each data point. The impedance kept increasing until reaching a steady plateau. The transition time constant for the impedance increase was around 1286 seconds, which should include the time required for T3 diffusing from the bulk solution to the electrode surface, and the hybridization time required for forming a layer of dsDNA.

As control experiments, we added 1.6 μL of 100 μM T3 solution into the 160 μL electrolyte with a bare glassy carbon electrode that has not been modified with P3. To compare bare electrode with P3 modified electrode, we normalized $|Z|$ with $|Z_0|$ (impedance of the first data point). We found that the trends in the change of the total impedance of these two electrodes are similar. But during period III, $|Z|$ of the electrode modified with P3 increased back to 99.5% of $|Z_0|$, while for bare electrode, it only increased back to 96% of $|Z_0|$. Besides the percentage of change, the time required to reach the steady state was much longer for the bare electrode, upto 1781 seconds. The target DNA may stick onto glassy carbon surface through nonspecific physical adsorption.

In another control experiment, we added 1.6 μL of 0.067X PBS buffer into the cell which was already filled with 160 μL of 0.067X PBS buffer in contact with an electrode modified with P3. In period III, the impedance monotonically decreased and never came back.

3.3 Hairpin DNA opening and closing driven by electric field

3.3.1 Characterization of VACNF chip

As-grown VACNF chip (Figure 3-24-A) was placed in a CVD chamber for SiO_2 encapsulation. After 7 hours, the individual CNF was fully coated by SiO_2 (Figure 3-24-B). Before RIE, the chip was planarized by mechanically polishing with 0.05 μm alumina slurry. Using ~39 minutes of RIE, it was successful to expose desired amount of CNF tips. The SEM of VACNF chip indicated that a sample with low density of exposed CNF tips (Figure3-24-C). CV plot further confirmed the low density by showing a sigmoidal shape (Figure3-24-D).

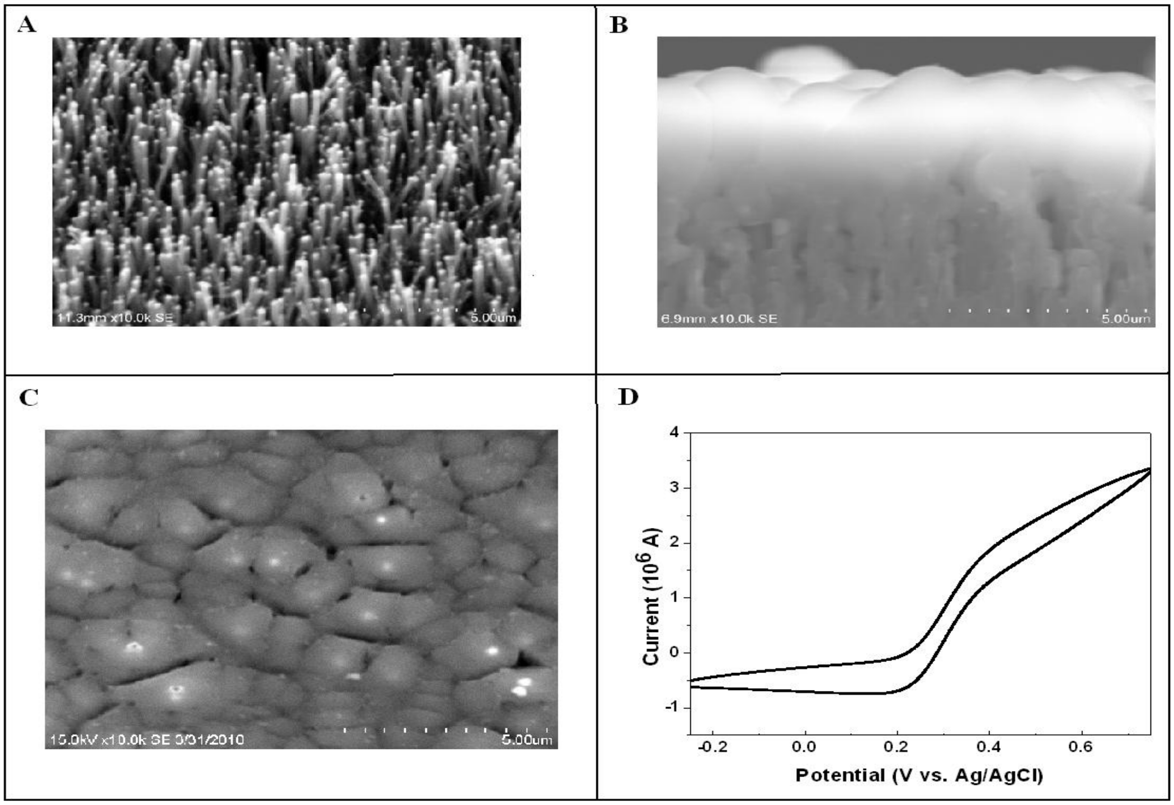

Figure 3-24 Characterization of VACNF chip. A. SEM image of as-grown VACNF; B SEM of SiO_2 encapsulated VACNF chip. C. SEM image of a low density CNF chip after chemical and mechanical polishing. D. CV plot of this chip in 1 mM $K_4Fe(CN)_6$ with 1 M KCl. Scan rate 0.05 V/ sec.

3.3.2Hairpin DNA opening and closing on VACAF chip and glassy carbon.

On glassy carbon we also observed the hairpin DNA opening and closing when applied enough negative bias. An alternating potential train was applied. The positive bias was hold at 0.2 V vs.OCP, and the negative bias systematically decreased from -0.2 V to -0.6 V vs. OCP (Figure 3-25). At -0.2V, there is no fluorescence modulation which means that the electric field generated by -0.2 V was not strong enough to force the stem arms to dehybridize. At -0.4 V, there started to show small fluorescence signal change along with the potential steps. At -0.6 V, the hairpin DNA was clearly dehybridized at the negative potential and rehybridize at the positive potential. The trend of the fluorescence signal kept increasing which indicated that at -0.6 V, the stem arms were dehybridized, but at +0.2 V, the rehybridization was not as strong as dehybridization. After one negative step and one positive potential step, the net effect was that most hairpin DNAs were dehybridized.

On the other hand, the negative bias was hold at -0.6 V vs. OCP, and the positive bias was systematically increased from +0.2 V to +0.8 V (Figure 3-25). As showed in Figure, a more positive potential closed the hairpin DNA more efficiently. The open and close of hairpin structure reached equivalent when applying symmetrical potential steps (-0.6 V and +0.6V). If the positive potential overwhelmed the negative potential (+0.8V and -0.6V), the net effect of the potential steps was hairpin DNA closing.

Unlike glassy carbon chip at which the fluorescence image was uniform throughout the 20 μm X 20 mm area, the image of CNF has some brighter spots indicated that DNA aggregated on the CNF tips (Figure 3-26-A). We also observed hairpin DNA open and close in synchronization with switching the potential steps at the CNF tips (Figure 3-26-B).

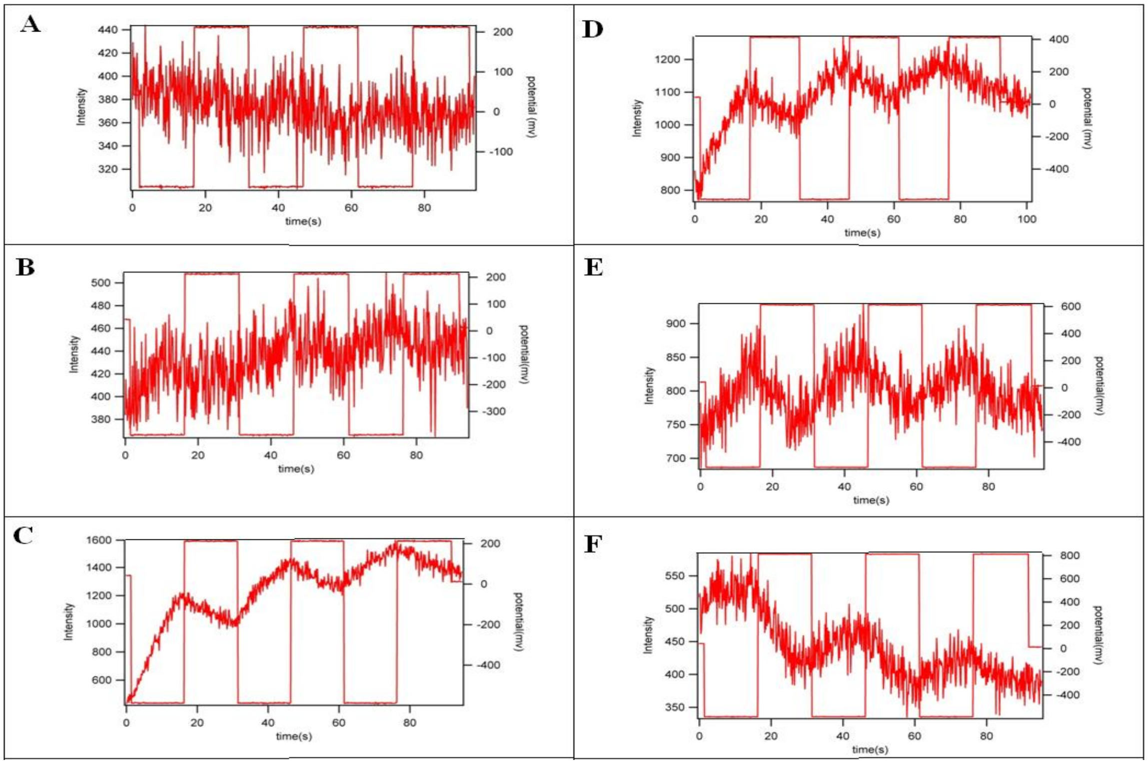

Figure 3-25 Hairpin DNA open and close on glassy carbon in 0.2 X PBS buffer. A, B, C, the positive potential hold at 0.2V, the negative potential were -0.2 V, -0.4 V and -0.6 V. D, E, F, the negative potential hold at -0.6 V, the positive potential were +0.4 V, +0.6 V, and +0.8 V. Laser power was 2 mW.

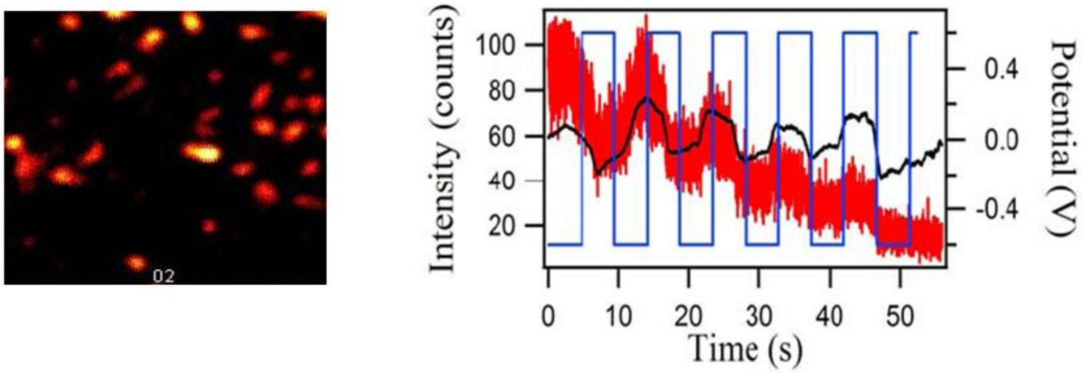

Figure 3-26 Variation in the fluorescence from a single point over a hairpin DNA-labelled NEA as the potential is switched between -0.6 and +0.6V. This experiment was performed in a solution of 0.01x PBS buffer with 1mM $MgCl_2$. The raw data is shown in red and smoother, background corrected data is shown in black. The approximate potential applied to the NEA is shown in blue.

Chapter 4 - Conclusion and Future research

In these studies for glassy carbon electrode, we have demonstrated that the strong electric field (200-2000 kV/cm) generated within the electric double layer (thickness 1- 10 nm) in low ionic strength solutions (1 mM to 30 mM salt) could manipulate the orientation of dsDNAs that are end tethered on glassy carbon. Also this strong electric field resonance at high frequency (5000 Hz) could be applied on monitoring DNA hybridization in real time by AC impedance spectroscopy with glassy carbon. We found the electric field strength play an important role in opening the hairpin DNA stem. The field strength must be above a threshold to open hairpin DNA effectively (-0.6 V vs. OCP in 0.2 X PBS).

For CNF nanoelectrodes, we have proved that they could be applied to develop DNA hybridization sensor using normal EIS method. The charge transfer resistance (R_{ct}) could be used to indicate ssDNA hybridization into dsDNA at the electrode surface. Also, we explored detection of open and close of hairpin DNA attached on CNF tips by fluorescence technique.

Till now, we derived the tilt angle from the fluorescence profile to describe the dsDNA reorientation by adopting the dipole-surface energy transfer theory. This derivation is based on some assumptions that need further experimental support. We assumed that -0.2 V vs.OCP is strong enough to repel dsDNA to cause it to fully stand up. This assumption can be validated by measuring the fluorescence signal when the amplitude of the negative potential step is gradually changed. We assumed that the variations of DNA density from chip to chip and the experimental setup (alignment, laser power et al.) are negligible. An external standard (fluorescence spheres) may be useful to calibrate the fluorescence signal and reduce potential errors.

We established a simple model to address the rearrangement of electric double layer and to explain the origins of the dsDNA reorientation. But the rigorous role of end-tethered polycharged dsDNA in EDL is not clear. Computational study which could simulate the Brownian motion of ions, dsDNA, solution, the formation and rearrangement of electric double layer, and the surface structure of glassy carbon (high portion of perfect fullerene, low portion of broken C-C bond) should be helpful to understand the origins the slow dsDNA reorientation.

We have proved that the patterned CNF array could be used to detect DNA hybridization. For a real sensor application, the detection limit needs to be determined, and multichannel detection should be explored.

The advantages of nanomaterials should be explored in more detailed way by comparing with glassy carbon. For example, the enhancement of electric field at VACNF is expected to open and close hairpin DNA more efficiently than macroscopic glassy carbon electrodes. VACNF NEAs should be able to detect DNA hybridization in real-time much faster than glassy carbon due to the hemisphere diffusion model and enhancement of electric field of VACNF.

References

(1) Fung, D. Y. C. *Food Science & Technology* **2008**, *22*, 21-23.

(2) Newman, W. Egg Recall Expanded After Salmonella Outbreak. *http://www.nytimes.com/2010/08/19/business/19eggs.html*.

(3) Abubakar, I.; Irvine, L.; Aldus, C. M.; Wyatt, G. M.; Fordham, R.; Schelenz, S.; Shepstone, L.; Howe, A.; Peck, M.; Hunter, P. R. *Health Technology Assessment* **2007**, *11*.

(4) Sassolas, A.; Leca-Bouvier, B. D.; Blum, L. J. *Chemical Reviews* **2008**, *108*, 109-139.

(5) Privett, B. J.; Shin, J. H.; Schoenfisch, M. H. *Analytical Chemistry* **2010**, *82*, 4723-4741.

(6) Gooding, J. J. *Electroanalysis* **2002**, *14*, 1149-1156.

(7) Daniels, J. S.; Pourmand, N. *Electroanalysis* **2007**, *19*, 1239-1257.

(8) Chen, J. H.; Zhang, J.; Huang, L. Y.; Lin, X. H.; Chen, G. N. *Biosens. Bioelectron.* **2008**, *24*, 349-355.

(9) Ozkan-Ariksoysal, D.; Tezcanli, B.; Kosova, B.; Ozsoz, M. *Anal. Chem.* **2008**, *80*, 588-596.

(10) Zhang, Y. L.; Wang, Y.; Wang, H. B.; Jiang, J. H.; Shen, G. L.; Yu, R. Q.; Li, J. H. *Anal. Chem.* **2009**, *81*, 1982-1987.

(11) Wei, D.; Bailey, M. J. A.; Andrew, P.; Ryhanen, T. *Lab on a Chip* **2009**, *9*, 2123-2131.

(12) Nguyen-Vu, T. D. B.; Chen, H.; Cassell, A. M.; Andrews, R. J.; Meyyappan, M.; Li, J. *Ieee Transactions on Biomedical Engineering* **2007**, *54*, 1121-1128.

(13) Nguyen-Vu, T. D. B.; Chen, H.; Cassell, A. M.; Andrews, R.; Meyyappan, M.; Li, J. *Small* **2006**, *2*, 89-94.

(14) Gasparac, R.; Taft, B. J.; Lapierre-Devlin, M. A.; Lazareck, A. D.; Xu, J. M.; Kelley, S. O. *J. Am. Chem. Soc.* **2004**, *126*, 12270-12271.

(15) Bard, A. L.; Faulkne, L. R. In *Electrochemcial Methods: Fundmentals and Applications;* Wiley India (P.) Ltd: Delhi, 2010.

(16) Harris, D. C. In *Quantitative Chemical Analysis;* W. H. Freeman and Company: New York, 2007.

(17) Arinaga, K.; Rant, U.; Knezevic, J.; Pringsheim, E.; Tornow, M.; Fujita, S.; Abstreiter, G.; Yokoyama, N. *Biosensors & Bioelectronics* **2007**, *23*, 326-331.

(18) Kaiser, W.; Rant, U. *Journal of the American Chemical Society* **2010**, *132*, 7935-7945.

(19) Rant, U.; Arinaga, K.; Fujita, S.; Yokoyama, N.; Abstreiter, G.; Tornow, M. *Nano Letters* **2004**, *4*, 2441-2445.

(20) Rant, U.; Arinaga, K.; Scherer, S.; Pringsheim, E.; Fujita, S.; Yokoyama, N.; Tornow, M.; Abstreiter, G. *Proceedings of the National Academy of Sciences of the United States of America* **2007**, *104*, 17364-17369.

(21) Rant, U.; Arinaga, K.; Tornow, M.; Kim, Y. W.; Netz, R. R.; Fujita, S.; Yokoyama, N.; Abstreiter, G. *Biophysical Journal* **2006**, *90*, 3666-3671.

(22) Rant, U.; Pringsheim, E.; Kaiser, W.; Arinaga, K.; Knezevic, J.; Tornow, M.; Fujita, S.; Yokoyama, N.; Abstreiter, G. *Nano Letters* **2009**, *9*, 1290-1295.

(23) Sendner, C.; Kim, Y. W.; Rant, U.; Arinaga, K.; Tornow, M.; Netz, R. R. *Physica Status Solidi a-Applications and Materials Science* **2006**, *203*, 3476-3491.

(24) Spuhler, P. S.; Knezevic, J.; Yalcin, A.; Bao, Q. Y.; Pringsheim, E.; Droge, P.; Rant, U.; Unlu, M. S. *Proceedings of the National Academy of Sciences of the United States of America* **2009**, *107*, 1397-1401.

(25) Dulkeith, E.; Morteani, A. C.; Niedereichholz, T.; Klar, T. A.; Feldmann, J.; Levi, S. A.; van Veggel, F. C. J. M.; Reinhoudt, D. N.; Moller, M.; Gittins, D. I. *Phys. Rev. Lett.* **2002**, *89*.

(26) Cnossen, G.; Drabe, K. E.; Wiersma, D. A. *J. Chem. Phys.* **1993**, *98*, 5276-5280.

(27) Jennings, T. L.; Singh, M. P.; Strouse, G. F. *J. Am. Chem. Soc.* **2006**, *128*, 5462-5467.

(28) Sen, T.; Sadhu, S.; Patra, A. *Appl. Phys. Lett.* **2007**, *91*.

(29) Stryer, L.; Haugland, R. P. *Proc. Natl. Acad. Sci. U. S. A.* **1967**, *58*, 719-726.

(30) Sen, T.; Jana, S.; Koner, S.; Patra, A. *Journal of Physical Chemistry C* **2010**, *114*, 707-714.

(31) Kroto, H. W.; Heath, J. R.; Obrien, S. C.; Curl, R. F.; Smalley, R. E. *Nature* **1985**, *318*, 162-163.

(32) Banks, C. E.; Compton, R. G. *Analytical Sciences* **2005**, *21*, 1263-1268.

(33) Banks, C. E.; Davies, T. J.; Wildgoose, G. G.; Compton, R. G. *Chemical Communications* **2005**, 829-841.

(34) McCreery, R. L. *Chemical Reviews* **2008**, *108*, 2646-2687.

(35) Halpin, M. K.; Jenkins, G. M. *Proceedings of the Royal Society of London Series A-Mathematical and Physical Sciences* **1969**, *313*, 421-431.

(36) Pocard, N. L.; Alsmeyer, D. C.; Mccreery, R. L.; Neenan, T. X.; Callstrom, M. R. *J. Mater. Chem.* **1992**, *2*, 771-784.

(37) Yamada, S.; Sato, H. *Nature* **1962**, *193*, 261-262.

(38) Kakinoki, J. *Acta Crystallogr.* **1965**, *18*, 578.

(39) Jenkins, G. M.; Kawamura, K.; Ban, L. L. *Proceedings of the Royal Society of London Series A-Mathematical and Physical Sciences* **1972**, *327*, 501-517.

(40) Harris, P. J. F. *Critical Reviews in Solid State and Materials Sciences* **2005**, *30*, 235-253.

(41) Harris, P. J. F. *Philosophical Magazine* **2004**, *84*, 3159-3167.

(42) Iijima, S. *Nature* **1991**, *354*, 56-58.

(43) Li, J.; Koehne, J. E.; Cassell, A. M.; Chen, H.; Ng, H. T.; Ye, Q.; Fan, W.; Han, J.; Meyyappan, M. *Electroanalysis* **2005**, *17*, 15-27.

(44) Li, J.; Ng, H. T.; Cassell, A.; Fan, W.; Chen, H.; Ye, Q.; Koehne, J.; Han, J.; Meyyappan, M. *Nano Letters* **2003**, *3*, 597-602.

(45) Ngo, Q.; Cassell, A. M.; Austin, A. J.; Li, J.; Krishnan, S.; Meyyappan, M.; Yang, C. Y. *IEEE Electron Device Lett.* **2006**, *27*, 622-622.

(46) Koehne, J.; Li, J.; Cassell, A. M.; Chen, H.; Ye, Q.; Ng, H. T.; Han, J.; Meyyappan, M. *Journal of Materials Chemistry* **2004**, *14*, 676-684.

(47) Koehne, J.; Chen, H.; Li, J.; Cassell, A. M.; Ye, Q.; Ng, H. T.; Han, J.; Meyyappan, M. *Nanotechnology* **2003**, *14*, 1239-1245.

(48) Nguyen, C. V.; Delzeit, L.; Cassell, A. M.; Li, J.; Han, J.; Meyyappan, M. *Nano Letters* **2002**, *2*, 1079-1081.

(49) Tyagi, S.; Kramer, F. R. *Nat. Biotechnol.* **1996**, *14*, 303-308.

(50) Bonnet, G.; Tyagi, S.; Libchaber, A.; Kramer, F. R. *Proc. Natl. Acad. Sci. U. S. A.* **1999**, *96*, 6171-6176.

(51) Taton, T. A.; Mirkin, C. A.; Letsinger, R. L. *Science* **2000**, *289*, 1757-1760.

(52) Bratu, D. P.; Cha, B. J.; Mhlanga, M. M.; Kramer, F. R.; Tyagi, S. *Proc. Natl. Acad. Sci. U. S. A.* **2003**, *100*, 13308-13313.

(53) Chen, A. K.; Davydenko, O.; Behlke, M. A.; Tsourkas, A. *Nucleic Acids Res.* **2010**, *38*, Article No.: e148.

(54) Li, X. M.; Huang, Y.; Guan, Y.; Zhao, M. P.; Li, Y. Z. *Anal. Chem.* **2006**, *78*, 7886-7890.

(55) Shaikh, F. A.; Ugaz, V. M. *Proc. Natl. Acad. Sci. U. S. A.* **2006**, *103*, 4825-4830.

(56) Wei, F.; Qu, P.; Zhai, L.; Chen, C. L.; Wang, H. F.; Zhao, X. S. *Langmuir* **2006**, *22*, 6280-6285.

(57) Drummond, T. G.; Hill, M. G.; Barton, J. K. *Nat. Biotechnol.* **2003**, *21*, 1192-1199.

(58) Lindholm-Sethson, B.; Nystrom, J.; Malmsten, M.; Ringstad, L.; Nelson, A.; Geladi, P. *Anal. Bioanal. Chem.* **2010**, *398*, 2341-2349.

(59) Macdonald, J. R. *Ann. Biomed. Eng.* **1992**, *20*, 289-305.

(60) Park, J.; Park, S. *Sensors* **2009**, *9*, 9513-9532.

(61) Lisdat, F.; Schafer, D. *Analytical and Bioanalytical Chemistry* **2008**, *391*, 1555-1567.

(62) AnonymousBasics of Electrochemical Impedance Spectroscopy. *http://www.gamry.com/App_Notes/Index.htm*.

(63) Lasia, A. In *Electrochemical Impedance Spectroscopy and Its Applications;* Modern Aspects of Electrochemistry; Kluwer Academic/Plenum Publishers: New York, 1999; Vol. 32, pp 143.

(64) AnonymousDNA strand length. *http://www.calctool.org/CALC/prof/bio/dna*.

(65) Anson, F. C.; Osteryoung, R. A. *J. Chem. Educ.* **1983**, *60*, 293-296.

(66) Bott, A. W.; Heineman, W. R. Chronocoulometry. *http://www.currentseparations.com/issues/20-4/20-4e.pdf*.

(67) Steel, A. B.; Herne, T. M.; Tarlov, M. J. *Anal. Chem.* **1998**, *70*, 4670-4677.

(68) Andreu, A.; Merkert, J. W.; Lecaros, L. A.; Broglin, B. L.; Brazell, J. T.; El-Kouedi, M. *Sens. Actuator B-Chem.* **2006**, *114*, 1116-1120.

(69) Siddiqui, S.; Arumugam, P. U.; Chen, H.; Li, J.; Meyyappan, M. *Acs Nano* **2010**, *4*, 955-961.

(70) Cassell, A. M.; Ye, Q.; Cruden, B. A.; Li, J.; Sarrazin, P. C.; Ng, H. T.; Han, J.; Meyyappan, M. *Nanotechnology* **2004**, *15*, 9-15.

(71) Koehne, J. E.; Chen, H.; Cassell, A. M.; Yi, Q.; Han, J.; Meyyappan, M.; Li, J. *Clin. Chem.* **2004**, *50*, 1886-1893.